



## Abstract

The diversity of slip processes occurring in the megathrust indicates that stress is highly variable in space and time. Based on GNSS and InSAR data, we study in depth the evolution of the interplate slip-rate along the Oaxaca subduction zone, Mexico, from October 2016 through August 2020, including the pre-seismic, coseismic and post-seismic phases associated with the 2020 Mw 7.4 Huatulco earthquake, to understand how different slip processes contribute to the stress accumulation in the region. Our results show that continuous changes in both the aseismic stress-releasing slip and the coupling produced a high stress concentration over the main asperity of the Huatulco earthquake and a stress shadow zone in the adjacent updip region. These findings may explain both the downdip rupture propagation of the Huatulco earthquake and its rupture impediment to shallower, tsunami-genic interface regions, respectively. Time variations of the interplate coupling around the adjacent 1978 Puerto Escondido rupture zone clearly correlate with the occurrence of the last three Slow Slip Events (SSEs) in Oaxaca far downdip of this zone, suggesting that SSEs are systematically accompanied by interplate coupling counterparts in the shallower seismogenic zone. In the same period, the interface region of the 1978 event experienced a remarkably high CFS built-up, imparted by the co-seismic and early post-seismic slip of the Huatulco rupture, indicating large earthquake potential near Puerto Escondido. Continuous monitoring of the interplate slip-rate thus provides a better estimation of the stress accumulation in the seismogenic regions where future earthquakes are likely to occur.

## Plain Language Summary

Advances in geodetic observational networks have made it possible to delimit the coupled portions of the plate interface that allow stress accumulation and where future large earthquakes might occur. These interplate coupling models are assumed to be time-invariant, thus producing constant interseismic deformation rates. However, different seismo-geodetic observations in the last 20 years have led to a more realistic and complex understanding of the seismic cycle that integrates a significant diversity of slow slip processes occurring in the plate interface that do not generate perceptible seismic waves. Among these aseismic slip phenomena, interplate coupling changes and slow slip events (SSEs) have a major bearing on how stresses accumulate and release at the plate interface. In this study, we analyze how these processes in the Oaxaca segment of the Mexican subduction zone contributed to the accumulation of stresses where the 2020 Mw. 7.4 Huatulco earthquake took place and the way interplate coupling at seismogenic depths changed with time during SSEs cycles, leading to a more realistic picture of the seismic potential in the region. This brings a valuable contribution for understanding the time-evolving seismic hazard in other subduction systems where similar aseismic slip processes also occur.

## 1 Introduction

Large earthquakes along subduction zones occur in regions known as asperities (Lay & Kanamori, 1981), which represent locked areas of the interplate contact where frictional resistance allows elastic stress to build up during tens to hundreds of years as a consequence of the relative plate motion. Under the simple concept of Coulomb failure criterion, an earthquake occurs when the shear stress overcomes the strength of the fault. Both stressing-rate and fault strength are parameters that vary in time and space during the megathrust earthquake cycle (Moreno et al., 2011). Therefore, understanding the tectonic and mechanical processes that cause these variations is essential to assess the seismic hazard in subduction zones.

Inter-seismic coupling maps obtained from geodetic observations have been widely used to identify heterogeneous, highly locked segments of the plate interface where large earthquakes take place (Chlieh et al., 2008; Loveless & Meade, 2011; Moreno et al., 2010; Perfet-

69 tini et al., 2010). Most of these estimations consider a steady-state long term deformation  
70 during the inter-seismic periods that results in a time invariant locking pattern. However,  
71 it has been observed that interplate coupling also varies with time (Heki & Mitsui, 2013;  
72 Melnick et al., 2017) and might be caused by different processes such as pore pressure  
73 transients (Cruz-Atienza et al., 2018; Materna et al., 2019; Warren-Smith et al., 2019) or  
74 dynamic stresses from regional earthquakes (Cruz-Atienza et al., 2021; Delorey et al., 2015;  
75 Materna et al., 2019).

76 During the inter-seismic period, a broad spectrum of tectonic processes occurs on the  
77 plate interface with distinctive spatiotemporal characteristics that play an important role  
78 to accommodate the strain along the megathrust. Among these processes, short-term and  
79 long-term slow slip events (SSEs), which are aseismic slip transients lasting from days to  
80 months, release the strain accumulation in the deeper and shallower segments of the plate  
81 interface (Beroza & Ide, 2011; Saffer & Wallace, 2015). Since their discovery, observations  
82 and theoretical models have shown that SSEs increase the stress in the adjacent seismogenic  
83 zone and may trigger damaging earthquakes (Obara & Kato, 2016; Segall & Bradley, 2012;  
84 Uchida et al., 2016; Voss et al., 2018). Moreover, it has been documented that major  
85 interplate earthquakes in different subduction zones are preceded by SSEs, although the  
86 actual mechanisms of their interaction remain under debate.

87 In the Mexican subduction zone, the recurrence of Mw 7+ interplate earthquakes is  
88  $\sim$ 30-50 years (Singh et al., 1981). In the deeper segment of the megathrust (30-50 km  
89 depth), long-term SSEs occur in Oaxaca and Guerrero with recurrence of  $\sim$ 1.5 and  $\sim$ 3.5  
90 years, respectively (Cotte et al., 2009; S. Graham et al., 2016). The last four Mw 7+  
91 interplate events in the Mexican subduction zone were preceded by SSEs in the downdip  
92 adjacent region: The 2014 Mw 7.4 Papanoa earthquake in Guerrero (Radiguet et al., 2016)  
93 and three more in Oaxaca, the 2012 Mw. 7.5 Ometepec earthquake (S. E. Graham et al.,  
94 2014a), the 2018 Mw 7.2 Pinotepa earthquake (Cruz-Atienza et al., 2021) and, as it will be  
95 shown later, the 2020 Mw 7.4 Huatulco earthquake. These observations suggest that the  
96 prevalent mechanism of the interaction between SSEs and unstable shallower regions in the  
97 Mexican subduction zone is the stress loading from adjacent slow slip processes. Although  
98 SSEs do not always trigger large earthquakes, they do interact periodically with the adjacent  
99 locked regions, thus contributing with the total stress built-up of the seismogenic zone.

100 Three years before the 2020 Huatulco earthquake, a complex sequence of SSEs and  
101 devastating earthquakes took place from June 2017 to July 2019 in central and southern  
102 Mexico, including the Mw 8.2 Tehuantepec and Mw 7.1 Puebla-Morelos earthquakes in 2017,  
103 and the Mw 7.2 Pinotepa earthquake in 2018, describing a cascade of events interacting with  
104 each other on a regional scale via quasi-static and/or dynamic perturbations (Cruz-Atienza  
105 et al., 2021). In Oaxaca, the plate interface slipped (aseismically) almost continuously for  
106 the whole two years period with at least two reactivations, one during the post-seismic  
107 relaxation of the Mw 7.2 Pinotepa earthquake, and the second one with the 2019 Oaxaca  
108 SSE.

109 Here we thoroughly study the evolution of the interplate slip-rate history in the Oaxaca  
110 segment during this unprecedented sequence including the pre-seismic, coseismic and post-  
111 seismic phases of the 2020 Huatulco earthquake with the aim of understanding how these  
112 processes contribute to the seismic potential in the region. We show that continuous and  
113 simultaneous monitoring of SSEs and the megathrust coupling provides a better estimation  
114 of the stress accumulation on the locked regions where future large earthquakes are expected  
115 to occur.

## 2 The 2020 Mw 7.4 Huatulco Earthquake

### 2.1 Coseismic slip inversion

On June 23, 2020, a shallow Mw 7.4 interplate thrust earthquake took place below the state of Oaxaca, Mexico (Fig. 1), with relocated hypocentral coordinates (latitude = 15.822, longitude = -96.125 and depth = 17.2 km, determined from seismic records at the station HUAT of the Mexican Servicio Sismológico Nacional (SSN), which is 7 km south of the epicenter) within the aftershock area of the 1965 Mw 7.5 earthquake, the last interplate rupture in this region (Chael & Stewart, 1982).

We combined nearfield GNSS and Interferometric Synthetic Aperture Radar (InSAR) data to obtain the coseismic slip distribution by means of ELADIN, a newly developed adjoint inversion method (Tago et al., 2021) (see Supporting Information). For the GNSS data we used high rate (1 s) time series to measure the coseismic static displacement at four stations near the epicenter (Figs. 1c and S1c-f). The displacement in Huatulco (HUAT station), the closest epicentral site, was carefully and independently estimated using GNSS, tide gauge and strong motion data, yielding very consistent values of 49 cm uplift and 40 cm seaward displacement (Figs. S1b and S1c). The InSAR line-of-sight (LOS) displacement map (Figs. 1b and S2) was generated from scenes taken before the earthquake, on June 19, and two days after the earthquake, on June 25, by the Sentinel satellite of the European Space Agency on ascending track 107. The InSAR data processing is described in the Supporting Information. For all slip inversions presented in this work we assumed the 3D plate interface geometry introduced by Cruz-Atienza et al. (2021) and discretized it, for the coseismic solutions, into subfaults with square horizontal projections of  $5 \times 5 \text{ km}^2$ .

To determine the optimal data weights for the joint inversion of GNSS and InSAR data we first inverted each data set individually. Both independent solution models produced almost a perfect data fit but significantly different slip distributions, as shown in Figs. S3a and S3b. Numerous joint inversion tests led us to optimal data weights (see Supporting Information) producing a final solution that owns the most prominent features of both independent models and satisfactorily explains the whole set of observations, with average GNSS and InSAR data errors of  $1.2 \pm 1.0 \text{ cm}$  and  $0.2 \pm 2.1 \text{ cm}$ , respectively (Figs. 1 and S3c).

Figure 1a features our preferred coseismic slip solution with two main patches, the most prominent downdip the hypocenter, between 21 and 32 km depth with peak value of 3.4 m, and a second one 45 km east-northeast, almost below the coast (peak value of 1.8 m), which differs from a recently published solution (Melgar et al., 2021) that did not integrate the closest (GNSS and strong motion) data and estimated a static uplift in Huatulco 6 cm higher than ours. Our slip solution explains both the uplift and seaward displacement there, and shows that no significant slip (i.e., larger than 1 m) took place offshore (Fig. 1). Furthermore, it clearly suggests a rupture directivity towards the north-northeast, essentially downdip from the hypocenter. Two more features stand out from our model: 1) The rupture ends abruptly updip and very close to the nucleation point, and 2) the downdip slip limit might correspond to the end of the locked segment of the megathrust, as observed for the 2018 Pinotepa Earthquake (Li et al., 2020), the 2012 Ometepec Earthquake (de México Seismology et al., 2013) and the aftershocks areas of regional interplate earthquakes (white patches in Fig. 1). We performed resolution tests following Tago et al. (2021) for the joint GNSS and InSAR inversion by means of mobile checkerboards tests with patch sizes of 20 km and different correlation lengths (L) (see Supporting Information). Our resolution analysis reveals that average restitution indexes (ARI, a metric that eliminates the resolution dependence on the checkerboard position) above 0.65 enclose the region where the two main slip patches are located (Fig. S4), which means that our preferred slip model, including these features, has a nominal error below 35% with respect to the actual slip distribution.

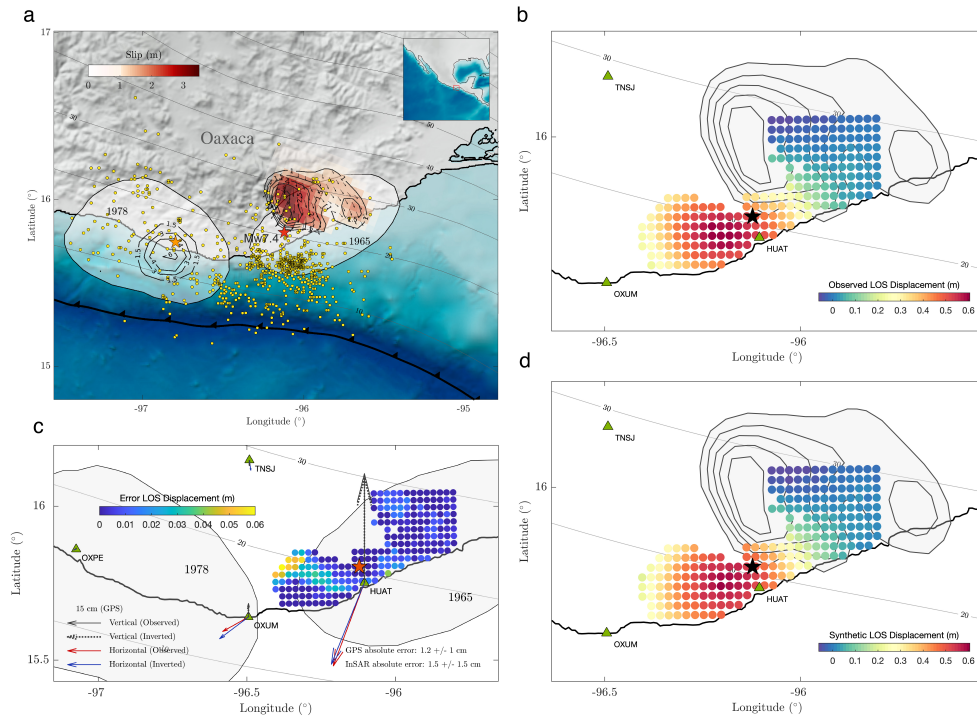


**Figure 1.** Coseismic slip inversion of the 2020 Mw 7.4 Huatulco earthquake. a Red colored region with black contours indicates the slip on the plate interface for our preferred joint GPS and InSAR slip inversion. Red and orange stars indicate the epicenters of the Huatulco and the 1978 Puerto Escondido earthquakes, respectively. Black contours around the 1978 Puerto Escondido epicenter represent the slip isolines (in m) determined by Mikumo et al. (2002). White shaded patches show the aftershock areas of the historic thrust earthquakes of 1965 and 1978. Yellow dots depict the first 50 days Huatulco earthquake aftershocks reported by the SSN. Gray contours indicate the iso-depths (in km) of the 3D plate interface used for the slip inversions in this study. b and d show the observed and synthetic line-of-sight (LOS) InSAR displacements, respectively (see Figure S2). c Misfit between observed and predicted LOS and GNSS surface displacements for our preferred slip model show in a (see Figure S3).

166 Whether the 2020 Huatulco earthquake is a repetition of two previous events that occurred in 1928 (Ms 7.6) and 1965 (Ms 7.4) is an important matter that goes beyond the scope of this work. However, since this question can be addressed by comparing far-field waveforms of the earthquakes, which are sensitive to the source depth (Chael & Stewart, 1982; Singh et al., 1984), we performed a supplementary inversion exercise where the interface was shifted 3.5 km upward to match our relocated hypocentral depth. The inversion yielded similar source characteristics as described above (Fig. S5) with some differences discussed in the Supporting Information that do not have a significant bearing on any subsequent analysis.

167  
168  
169  
170  
171  
172  
173  
174

## 2.2 The 2020 Oaxaca SSE that preceded the earthquake

Two months before the Huatulco earthquake, on mid-April 2020, three GNSS stations in Oaxaca (TNNP, TNNX and OAXA) changed their typical interseismic motion from roughly northeast to southwest, indicating a transient deformation associated with a SSE (light blue section in Fig. 2a). We used continuous displacement records on 13 permanent GNSS stations in Oaxaca (Fig. 2b) belonging to the SSN and Tlalocnet (Cabral-Cano et al., 2018), between September 2019 and the Huatulco earthquake date (Fig. S6) to simultaneously invert for the plate interface coupling (PIC, i.e.,  $1 - v/b$ , where  $v$  is the interplate slip rate,  $b$  is the plate convergence rate and  $v \leq b$ ) and any stress-releasing slip episode (i.e., SSEs) in successive time windows using ELADIN (Fig. 2b-d). To this end, we carefully corrected the displacement time series by fitting and removing seasonal effects as explained in detail in the Supporting Information (Fig. S7). For these and the next section inversions, the 3D plate interface was discretized with coarser subfaults of  $10 \times 10$  km<sup>2</sup>. Given both the interface geometry and the distribution of the GNSS stations in Oaxaca, we adopted the optimal regularization length of 40 km determined by Tago et al. (2021), which guarantees an inversion error under 50% (i.e., median restitution indexes higher than 0.5) for slip patches larger than  $\sim 80$  km length at most interface depths greater than 10 km (Fig. S8).

Figure 2e shows the main slow slip patch downdip of the 1978 Puerto Escondido earthquake region, between 25 and 50 km depth, with an equivalent moment magnitude  $M_w$  6.5 ( $M_o = 6.645 \times 10^{18}$  N\*m measured from the slip contour of 1 cm and assuming a shear modulus of 32 GPa). The location and magnitude of this SSE are consistent with previously reported SSEs in Oaxaca (Correa-Mora et al., 2008; Cruz-Atienza et al., 2021; S. Graham et al., 2016). It is also clear that the SSE did not penetrate the rupture area of the Huatulco earthquake. Instead, we observe a remarkable PIC evolution previous to the event close to its hypocentral region, where the interface decoupled around February-March (Fig. 2d) before getting fully coupled just before the earthquake (i.e., during the strongest SSE phase, Fig. 2e). This can also be seen directly in the GNSS time series at the stations closest to the epicenter, such as OXUM and HUAT (Fig. 2a), where we do not observe the SSE southward rebound before the earthquake. Something similar occurred in the hypocentral region of the 2018 Pinotepa earthquake ( $M_w$  7.2) 200 km west, where the seismicity rate also increased in the two months preceding the rupture (Cruz-Atienza et al., 2021). We carefully analyzed the foreshock seismicity starting from August 2016 in the hypocentral region of the Huatulco earthquake using the one-station template-matching procedure introduced by Cruz-Atienza et al. (2021) from continuous broadband records at the HUAT station (Fig. S9). However, unlike the observations of the 2018 Pinotepa earthquake, we did not find significant increase in the seismicity rate prior to the event that could shed further light on the rupture initiation mechanism.

Although the transient deformation produced by the SSE is noticeable from mid-April, the inter-SSE displacement trends in some stations started changing well before, around mid-February as observed in Figure 2a (red dashed lines), suggesting a gradual plate interface decoupling process at a regional scale preceding the SSE-induced crustal relaxation, which can be observed in Figs. 2b-d and 2f (see also Supplementary Movie S1). Before such decoupling process began (Fig. 2b), the downdip segment of the plate interface, between 25-50 km, was fully coupled while small SSE episodes were taking place in both the 2018 ( $M_w$  7.2) Pinotepa earthquake area and up-dip of the Huatulco earthquake rupture zone. In the following two months, there seems to have been an incipient downdip SSE propagation from south to north nearby Pinotepa (Supplementary Movie S1 and Figs. 2b-c). Then, in Figs. 2d and 2f we see how the segment downdip of the 1978 earthquake area is the last one to experience a PIC reduction (i.e., the interface slip starts accelerating but always below the plate convergence rate) leading to the main SSE patch occurrence in April-June, the months preceding the earthquake (Figs. 2e and 2f). All of these observations clearly demonstrate the regional-wide preparatory phase for the 2020 Oaxaca SSE.

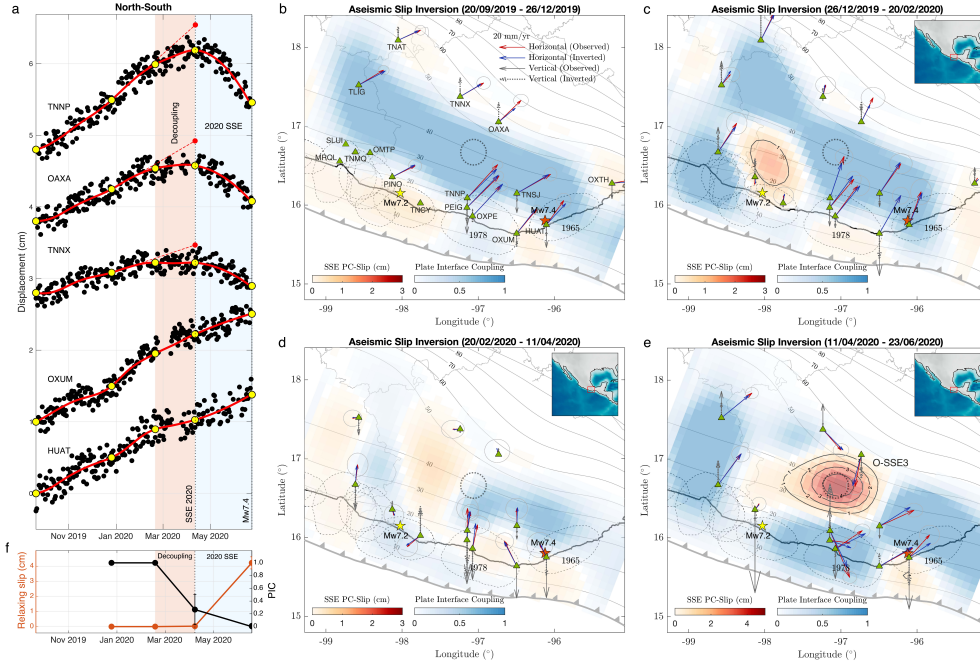


**Figure 2.** GNSS inversions of the 9-month deformation period prior to the June 23, 2020, Mw 7.4 Huatulco earthquake. a North-south GNSS time series in 5 selected stations. Yellow dots indicate the beginning and end of the four time-windows used for the slip inversions shown in b-e, and red dashed lines depict the inter-SSE displacement trend during the interface decoupling phase. b-e Inverted slip in the plate-convergence (PC) direction for all time windows. Slip contours are in centimeters. Red and yellow stars indicate the epicenters of the Huatulco and 2018 Pinotepa (Mw 7.2) earthquakes, respectively. Dashed regions are the aftershock areas of historic interplate earthquakes. Gray ellipses around the arrow tips are represent one standard deviations of the observed displacements. f Average and standard deviation (vertical bars) of the plate interface coupling (PIC) and relaxing slip in the region where the 2020 SSE developed (i.e., within the dotted black circle in b-e).

228 A common practice to isolate the deformation associated with slow slip transients is  
 229 to subtract the inter-SSE linear trend from the GNSS time series. The residual deformation  
 230 is then assumed to correspond to the strain released by the SSE (e.g. Bartlow et al.,  
 231 2011; Hirose et al., 2014; Radiguet et al., 2011). When doing this to invert for the slip  
 232 at the interface, the preparatory phase of the SSE (i.e., the slow decoupling process pre-  
 233 ceding the SSE relaxation) is mapped/interpreted as aseismic slip resulting in an elastic  
 234 crustal rebound (i.e., a stress drop). However, since this process instead reveals a gradual  
 235 decrease in the upper crustal stressing rate, such a misleading practice leads to a systematic  
 236 overestimation of the SSE-related surface displacements and, therefore, of the SSE equiva-  
 237 lent seismic moment with relevant implications in the scaling properties of slow earthquakes  
 238 and, more importantly, in the slip budget over several SSE cycles, which may be significantly  
 239 underestimated.

240 **2.3 Early post-seismic deformation**

241 We inverted the early post-seismic GNSS displacements (i.e., the first 2 months following  
 242 the earthquake discretized in 6 ten-day windows, Figs. 3a and S10b) produced by the

mainshock using the same parameterization for the ELADIN method as in the previous section. We then assumed that such displacements are only due to the afterslip on the plate interface, which is a reasonable approximation considering that the viscoelastic relaxation after a similar thrust event 260 km west, the 2012 (Mw 7.5) Ometepec earthquake, was negligible in a post-seismic period three times longer (S. E. Graham et al., 2014b).

Four main observations arise from the afterslip evolution of the Huatulco earthquake (Fig. 3b and Supplementary Movie S1): (1) the largest afterslip concentrates between 20 and 50 km depth overlapping with the main SSE patch preceding the earthquake (i.e., downdip from the 1978 rupture area) and where previous SSEs have been identified (Fig. 4a); (2) the maximum postslip area completely overlaps with the coseismic rupture area; (3) the afterslip spreads offshore up to the oceanic trench where most of aftershocks concentrate; and (4) the afterslip rate reaches its maximum value of 390 cm/year during the first 10 days following the earthquake (Supplementary Movie S1).

The complete overlap of coseismic and postseismic slip has been observed in the last three interplate thrust earthquakes (Mw 7) in Oaxaca, the 2012 (Mw 7.5) Ometepec (S. E. Graham et al., 2014b); the 2018 (Mw 7.2) Pinotepa (Cruz-Atienza et al., 2021) and the 2020 (Mw 7.4) Huatulco (this study) events, indicating that these seismogenic segments of the plate interface, with depth range between 10 and 30 km, can release elastic strain energy both seismically and aseismically. However, the propagation of the Huatulco earthquake afterslip to the trench is an interesting feature that clearly differs from the Pinotepa earthquake, whose afterslip stopped under the coast (i.e., at  $\sim 15$  km depth and without offshore propagation) (Figs. 4a and S11e-g). This observation suggests significant lateral variations in the mechanical and/or geometrical characteristics along the Oaxaca subduction zone, especially in the updip interface region.

The cumulative aseismic moment released during the first two months following the earthquake was  $1.808 \times 10^{20}$  N m, equivalent to a moment magnitude Mw 7.44, which is 24% larger than the coseismic moment. The high postseismic/coseismic moment ratio is also a common feature of the three Oaxaca events mentioned above, that significantly differs from the much lower estimate for the 2014 (Mw 7.4) Papanaoa thrust earthquake in Guerrero, where the postslip moment was 30% smaller than the corresponding coseismic value (Gualandi et al., 2017).

Another noteworthy features of the postseismic process in the region is that the Huatulco earthquake postslip did not penetrate the rupture area of the 1978 Puerto Escondido earthquake (dashed ellipse in Fig. 3b), which remained fully coupled during the two-month period. Unlike most of the preseismic phase (i.e., before April, Fig. 2e), the PIC in the 1978 rupture area remained fully locked after the earthquake (compare Figs. 2 and 3) suggesting significant dynamic implications for the accommodation of postseismic strain in the region.

### 3 Interplate slip-rate evolution in the Oaxaca subduction zone.

Before the occurrence of the Huatulco earthquake, a complex sequence of earthquakes and SSEs took place in an unusual way along the Mexican subduction zone from April 2017 to September 2019 due to the extremely large, unprecedented seismic waves from the Mw 8.2 Tehuantepec earthquake on September 8, 2017 (Cruz-Atienza et al., 2021). During this period, two large SSEs occurred in the downdip interface region of Oaxaca (namely the 2017 SSE (O-SSE1) and the 2019 SSE (O-SSE2)) where the recent 2020 SSE (O-SSE3) took also place (Figure 4a). Indeed, the plate interface slipped aseismically and continuously for two years from O-SSE1, experiencing two spontaneous reactivations in this period, one with the afterslip of the Pinotepa earthquake and the other with the O-SSE2 (Cruz-Atienza et al., 2021).

We corrected the GNSS displacement time series used by Cruz-Atienza et al. (2021) for seasonal effects from October 2016 to September 2019 as previously done in section 2.2 (Fig.

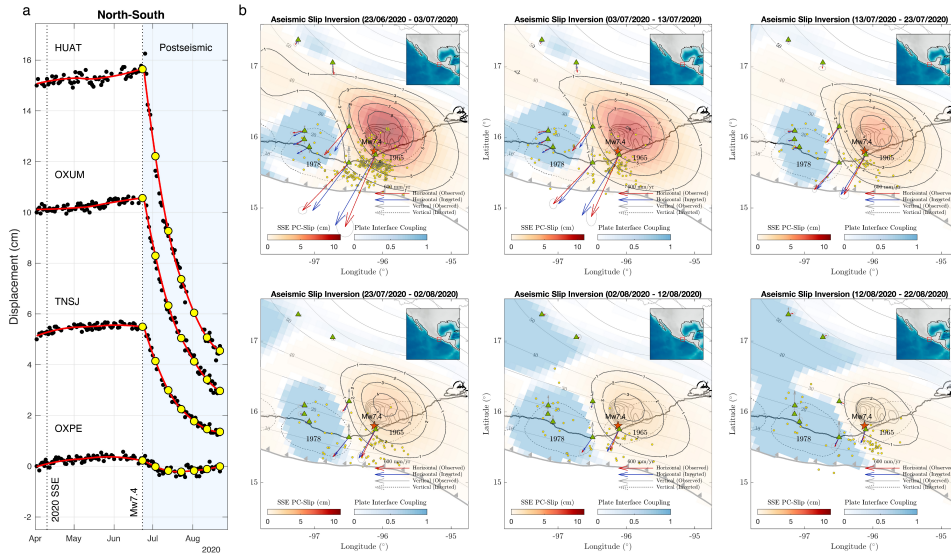


**Figure 3.** GNSS inversion of the postseismic deformation of the Huatulco earthquake. a North-south displacement GNSS time series in 4 selected stations. Yellow dots indicate the start and the end of the six 10-day windows used for the slip inversions shown in b. b Aseismic slip inversion for the two months following the Huatulco earthquake. Thick light gray contours are the coseismic slip shown in figure 1a.

293 S7) and inverted them for the interplate aseismic slip in greater detail along the Oaxaca  
 294 megathrust using the 17 GNSS stations shown in Figure 2b. The new inverted sequence is  
 295 shown in Figure S11 and Supplementary Movie S1. During the sequence, the plate interface  
 296 experienced remarkable changes of the PIC over time in the whole megathrust. To analyze  
 297 the long-term evolution of the aseismic slip before the Huatulco earthquake, we integrated  
 298 the new corrected slip sequence from October 2016 to September 2019 (Fig. S11) and the  
 299 subsequent sequence discussed in section 2.2 (from September 2019 to June 2020, Fig. 2),  
 300 and linearly interpolated the complete slip history every 30 days. To analyze our inversion  
 301 results, we also disaggregated the total slip into relaxing and stressing interface regions, i.e.,  
 302 into SSEs and afterslip regions where the slip rate is greater than the plates convergence  
 303 rate and, therefore, release elastic strain (e.g. red gradient zones in Figs. 2 and 3); and  
 304 regions under coupling regime, where the velocity of the interplate creep is less than or equal  
 305 to the plates convergence rate that grows eastward along the coast (DeMets et al., 2010)  
 306 and, therefore, accumulate elastic strain (e.g. blue gradient zones in Figs. 2 and 3).

307 Figures 2 shows the evolution of the relaxing slip on the plate interface along the trench  
 308 (i.e., projected into the green line of Figure 4a) averaged in two different depth ranges,  
 309 between 10-20 km depth (Fig. 4b) and between 20-30 km depth (Fig. 4c), encompassing the  
 310 rupture areas of the 2018 Pinotepa, 1978 Puerto Escondido and 2020 Huatulco earthquakes  
 311 (Fig. 4a). Figures 4b and 4c show that the Pinotepa earthquake afterslip (yellow areas)  
 312 dominates in the region for the analyzed period. However, there are other significant slip  
 313 episodes (i.e., short-term SSEs) most often in the shallow zone (within the 10-20 km depth  
 314 range) excluding the 1978 rupture zone.

315 To better analyze the interplate slip-rate variations we extracted the time series of the  
 316 slip evolution at six places of the plate interface (dashed blue circles with radius of 20 km in  
 317 Fig. 4a). Region A, over the rupture area of the Huatulco earthquake; Region B, over the

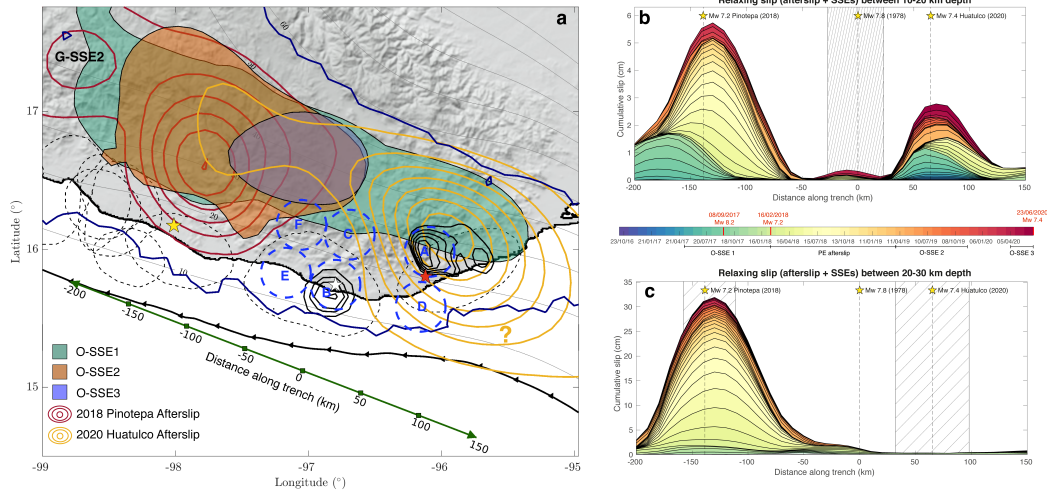


**Figure 4.** Aseismic slip at the plate interface in Oaxaca. a Summary of the aseismic slip processes (SSEs and afterslip) occurring from October 2016 to August 2020 in Oaxaca. Colored patches indicate the SSEs regions with slip values higher than 1.5 cm. Colored contours depict the afterslip of the Pinotepa and Huatulco earthquakes with slip isolines every 5 cm beginning with 1.5 cm. Dark blue contour indicates the region with restitution indexes higher than 0.5 from Figure S8b. Red, orange and yellow stars indicate the hypocenter of the Huatulco, the 1978 Puerto Escondido and the Pinotepa earthquakes, respectively. Dashed blue circles represents the areas where we analyze the evolution of the interplate slip rate and the CFS shown in Figs. 5 and S13. Green line indicates the along-trench profile where the evolution of the aseismic slip and CFS on the plate interface is analyzed in b and c and Figs. 6 and 7. b and c show the evolution of the relaxing aseismic slip (SSEs and afterslip) along the trench within the seismogenic zone averaged between 20-30 and 10-20 km depth, respectively. Hatched regions show the interplate segments with the highest moment release of the 2018 Pinotepa, 1978 Puerto Escondido and 2020 Huatulco earthquakes. Stars and dashed black lines indicate the along-trench coordinate of the hypocenters.

318 rupture area of the 1978 Puerto Escondido earthquake as estimated by Mikumo et al. (2002);  
 319 Region C, downdip from the rupture area of the Puerto Escondido earthquake; Region D,  
 320 updip from the Huatulco earthquake where most of its aftershocks are located; and Regions  
 321 E and F, west and northwest of the Puerto Escondido earthquake. Figures 5 and S12 show  
 322 the evolution of the mean total aseismic slip (black line), the creeping (yellow line), the  
 323 relaxing slip (red line) and the PIC (blue line) within each of the six circular regions.

324 In the Huatulco rupture area (Region A, Fig. 5a), the largest contribution to the total  
 325 slip is due to creeping except for a period after the Mw 8.2 Tehuantepec earthquake, when  
 326 aseismic stress release occurred during the late phase of the O-SSE1 (see Figures 4a and  
 327 S11c). This phase of the O-SSE1 was indeed triggered by the quasistatic and dynamic  
 328 stresses produced by the great Tehuantepec event as demonstrated by Cruz-Atienza et al.  
 329 (2021). In this region, PIC is highly variable over time and there is no clear correlation  
 330 with the occurrence of SSEs in Oaxaca that, except for the late phase of the O-SSE1 (Fig.  
 331 S11c), all occurred more than 100 km northwest from this region. We also find a gradual  
 332 decrease of PIC down to values of 0.1-0.2 at the end of the afterslip period of the Pinotepa  
 333 earthquake that eventually recovers during the O-SSE2 to remain high until the Huatulco  
 334 earthquake occurs, with values ranging between 0.7-1.0.

335 In the 1978 rupture area (Region B, Fig. 5b) there is no significant evidence of aseismic  
 336 stress release, so the total slip is only associated with creeping. In this region, PIC changes  
 337 correlate remarkably well with the occurrence of downdip SSEs in Oaxaca even though these  
 338 events did not penetrate the region. During the SSEs, PIC gradually increases to values of  
 339 0.7-0.8 in the initial stage of every SSE and then decreases in their final stage to remain  
 340 relatively low, with values down to 0.2-0.4 observed during the inter-SSE periods. This  
 341 remarkable behavior, which suggests a non-intuitive interaction between deep SSEs and the  
 342 coupling regime in the shallower seismogenic zone, is also found in Region E (Fig. S12c),  
 343 west of the 1978 rupture area.

344 To the east and thus offshore (and updip) the Huatulco earthquake (Region D, Fig.  
 345 S12b) we find a different and more consistent low PIC value across the whole studied period  
 346 with the exception of a prominent increase after the Tehuantepec earthquake, which might  
 347 be associated with the stress shadow produced in this specific spot by the great Mw8.2  
 348 rupture (Suárez et al., 2019; Cruz-Atienza et al., 2021). The red curve indicates that there  
 349 are small and persistent short-term, episodic SSEs in this offshore region over time that can  
 350 also be appreciated in Figures 4b and S11. Such a particular behavior is consistent with the  
 351 significant afterslip that swept that area into the trench after the Huatulco earthquake (Fig.  
 352 3). These observations suggest that frictional properties of this offshore region are prone to  
 353 release aseismically a fraction of the accumulated stress, as recently found in the Guerrero  
 354 seismic gap (Plata-Martínez et al., 2021).

355 Finally, downdip from the 1978 rupture area (Regions C and F, Figs. S12a and S12d)  
 356 we observe a complicated PIC evolution because of its proximity to the deep SSEs region.  
 357 During the occurrence of SSEs, PIC reductions begin well before the silent events, meaning  
 358 that creeping in some subfaults of these regions accelerates before the relaxing slip invades  
 359 them (see how the blue curves start decreasing before the red curves start growing). These  
 360 observations indicate that SSEs might partly penetrate these seismogenic depths (20 -30  
 361 km) (see also Figure 4a).

#### 362 **4 Implications of SSEs and PIC changes on the stress built-up**

363 Variations in the interplate aseismic slip rate have important implications for both  
 364 friction and the stress build-up along the megathrust. We estimated the Coulomb Failure  
 365 Stress (CFS) changes (Nikkhoo and Walter (2015), see Supporting Information) produced by  
 366 the relaxing slip (SSEs and afterslip) and the interplate coupling to elucidate how the stress  
 367 evolves along the Oaxaca segment. For this analysis we have also included the coseismic

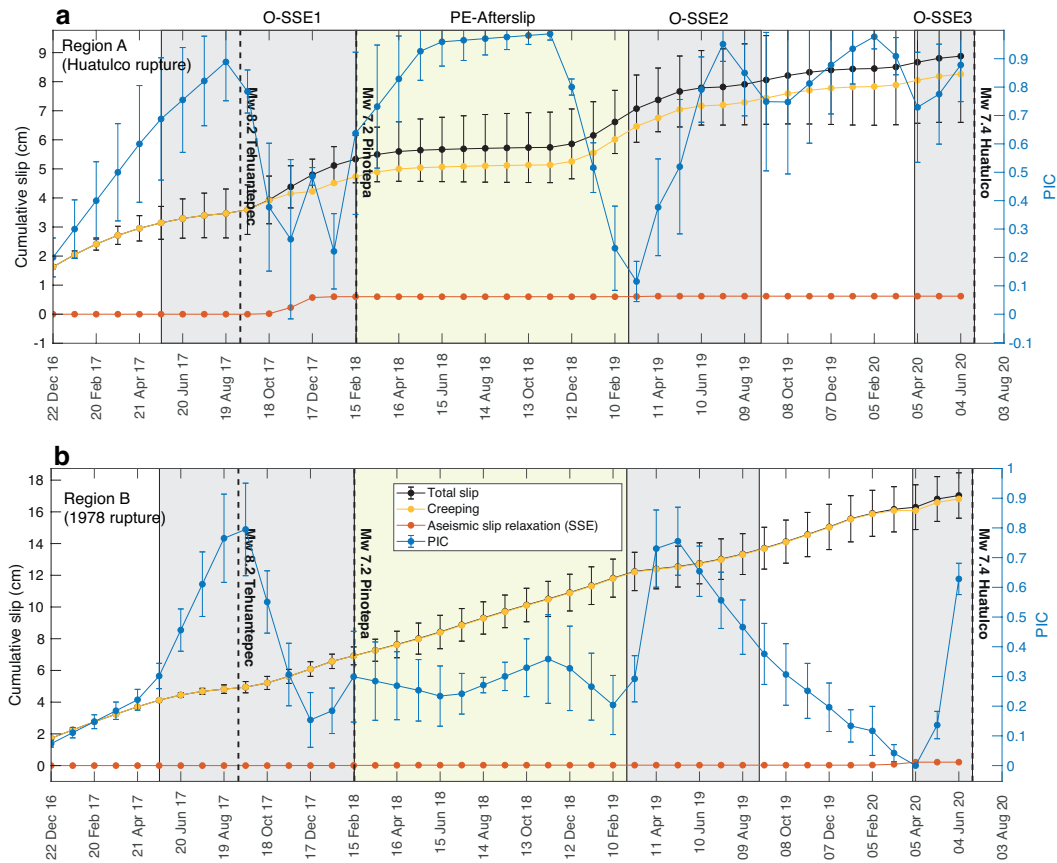


**Figure 5.** Detailed evolution of the aseismic slip in the seismogenic segment of Oaxaca. Time series show the cumulative total slip, creeping (slip under coupling regime), relaxing slip (SSEs) and plate interface coupling (PIC) in (a) Region A (the Huatulco rupture area) and (b) Region B (the 1978 Puerto Escondido rupture area) (see Figure 4). Gray rectangles indicate the time windows of the downdip SSEs in Oaxaca. The light-yellow rectangle depicts the timespan of the 2018 Pinotepa earthquake afterslip in the region.

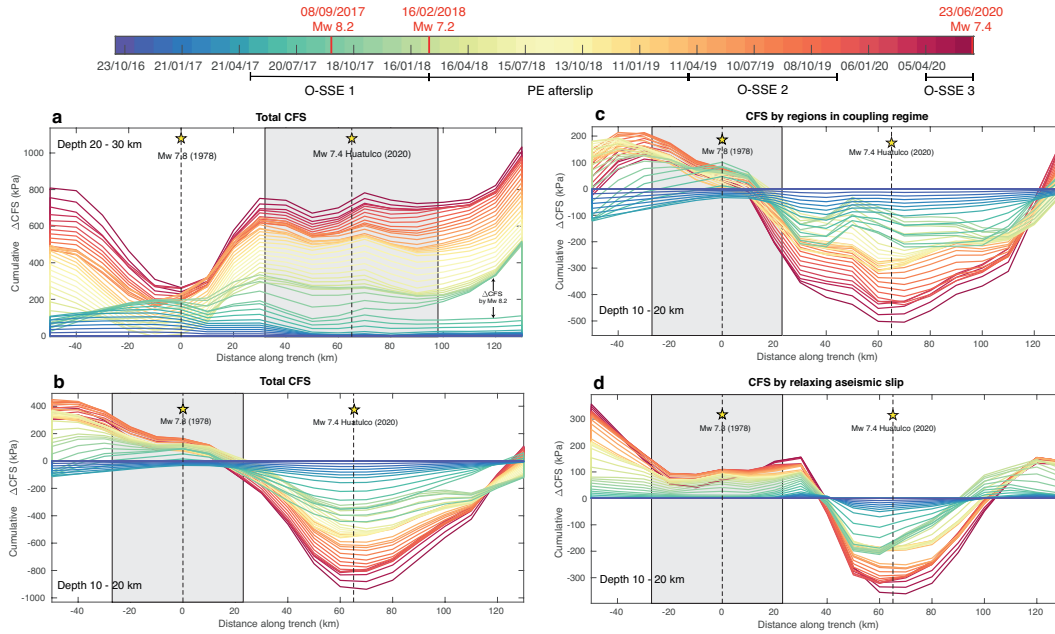


**Figure 6.** Evolution of the CFS in the seismogenic segment of Oaxaca. Evolution of the total CFS along the trench for every 30 days averaged between a 20-30 km and b 10-20 km depth. Gray rectangles show the interplate segments with the highest moment release of the 2020 Huatulco earthquake and the 1978 Puerto Escondido event (Mikumo et al., 2002). c and d show the evolution of the CFS for the band between 10-20 km depth split into the contributions from regions in coupling regime and the relaxing aseismic slip, respectively.

368 stresses imparted by the Tehuantepec (Cruz-Atienza et al., 2021), Pinotepa and Huatulco  
 369 earthquakes. Figures 6a and 6b show the average cumulative CFS every 30 days from  
 370 October 2016 up to the moment of the Huatulco event along the trench (i.e., projected onto  
 371 the green line in Figure 4a) for two different depth ranges encompassing the rupture areas of  
 372 the 2020 Huatulco (between 20 and 30 km depth, Fig. 6a) and the 1978 Puerto Escondido  
 373 (between 10 and 20 km depth, Fig. 6b) earthquakes. It is important to note that these  
 374 estimates of the CFS are the result of stress contributions from the whole plate interface  
 375 and not just from the sub-faults delimited by the depth ranges.

376 As expected, the CFS cumulative rate is highly variable over time and along the trench.  
 377 For the deeper region (Fig. 6a), we observe that despite the great variations of the slip-  
 378 rate on the megathrust, the CFS in Huatulco always increased up to values ranging from  
 379 600 to 800 kPa. We also observe a significant CFS contribution of  $\sim 100$  kPa induced  
 380 by the Mw8.2 Tehuantepec earthquake in the eastern limit of the Huatulco rupture zone  
 381 that exceeds 300 kPa further to the east. For the shallower region (Fig. 6b), the CFS  
 382 systematically decreases and remains negative right updip of the Huatulco rupture reaching  
 383 values of  $\sim -900$  kPa. Such large negative CFSs are associated with both the stress shadows  
 384 produced by neighboring strong coupled segments (e.g., the 1978 earthquake area) and the  
 385 periodic stress release by short-term SSEs in this offshore segment (Figs. 4b). This can be  
 386 seen in Figures 6c and 6d, where we disaggregate the stress changes due to the coupled and  
 387 relaxing interface regions, respectively. To the west, in the 1978 rupture area (Fig.6b), we  
 388 find the opposite situation. The CFS always increased to values between 100 and 400 kPa,  
 389 which are approximately half of the CFS estimates downdip of this segment (Fig. 6a).

Figure S13 shows both the long-term and inter-SSE time-invariant interplate coupling models estimated by Radiguet et al. (2016) (personal communication) together with their associated CFS change rate. Both models produce large stressing rates mainly in the coupled segment of the 1978 earthquake region. However, they also produce large stress shadows in the adjacent, less coupled regions (both along-dip and along-strike) such as in the Pinotepa and Huatulco rupture zones. Although these time-invariant coupling models may lack some observational coverage compared to the present investigation, they share similar features (though not all) to those found by Rousset et al. (2016) for the inter-SSE regime, which incorporates all available GPS observations in the region (compare Figure S13c and Figure 3B of Rousset et al. (2016)).

In contrast, our aseismic time-evolving slip model predicts a very different scenario. Figure 7a shows the cumulative CFS at the time of the Huatulco earthquake including contributions of all aseismic slip processes imaged in the megathrust during more than 3.5 years preceding the event (from October 2016 to June 23, 2020). A simple inspection reveals large differences in the stress build-up pattern with respect to the time-invariant models (Fig. S13), especially in both the Huatulco and Pinotepa rupture areas, and east-southeast of the 1978 earthquake zone. The bottom four panels of Figure 7 show the cumulative (trench-perpendicular average) CFS along the trench for the same two depth ranges analyzed earlier. The left column shows the cumulative CFS at the time of the Huatulco earthquake, while the right column shows the same quantity plus the coseismic and postseismic stress increments.

In the deeper region at the moment and within the rupture area of the Huatulco earthquake (Fig. 7b), the CFS from our time-evolving slip model (blue area) indicates more than double the CFS predicted by the inter-SSE coupling model by Radiguet et al. (2016) (yellow area), while their long-term coupling model (orange area) predicts even negative CFS values (i.e., no earthquake potential). Downdip of the 1978 rupture area, the CFS predicted by the three models are consistent (values ranging between 200 and 300 kPa), but to the west of this region our model again predicts very different stress concentrations, which are twice the CFS predicted by the inter-SSE coupling model. When adding the CFS imparted by the Huatulco earthquake and its postseismic afterslip (Fig. 7e), our estimate abruptly increases right downdip of the 1978 rupture area, from about 300 kPa to over 1.3 MPa. A significant fraction of this value is due to the persistently high coupling in this region throughout the post-seismic phase (Fig. 3). This large segment west of the Huatulco rupture (Region C in Fig. 4a) might be then very prone to a future earthquake, as has occurred in neighboring regions over the deep part of the locked zone where the last two interplate earthquakes in Oaxaca (the Pinotepa and Huatulco events) took place, with most of their seismic moment released below 20 km (Fig. 1a and Li et al. (2020)).

In the shallower region, the time-invariant coupling models predict higher CFS values over the 1978 rupture area than our time-evolving slip model before the Huatulco rupture (Fig. 7c). Only when adding the coseismic and postseismic stresses induced by the earthquake, the inter-SSE model prediction becomes similar to ours in the eastern part of the rupture area of the 1978 Puerto Escondido earthquake (Fig. 7f). Updip of the Huatulco rupture area (Fig. 7c), only our time-evolving model predicts a large CFS deficit, which is fully compensated (reaching positive values around 700 kPa) by the coseismic and postseismic deformations produced by the Huatulco earthquake (Fig. 7d).

We can therefore distinguish three major differences between our time-evolving CFS estimates and those from the time-invariant coupling models introduced by Radiguet et al. (2016): (1) very high stress concentration over the rupture area of the Huatulco earthquake before the event predicted only by our model, (2) absolute CFS values between 20 and 30 km depth at least twice as high in our model, and (3) a large stress shadow zone updip the Huatulco rupture before the event that is absent in both time-invariant models.

We now analyze in depth the CFS evolution in the Huatulco and 1978 rupture areas produced by our time-evolving interplate slip-rate model. Figures S14a and S14b show the

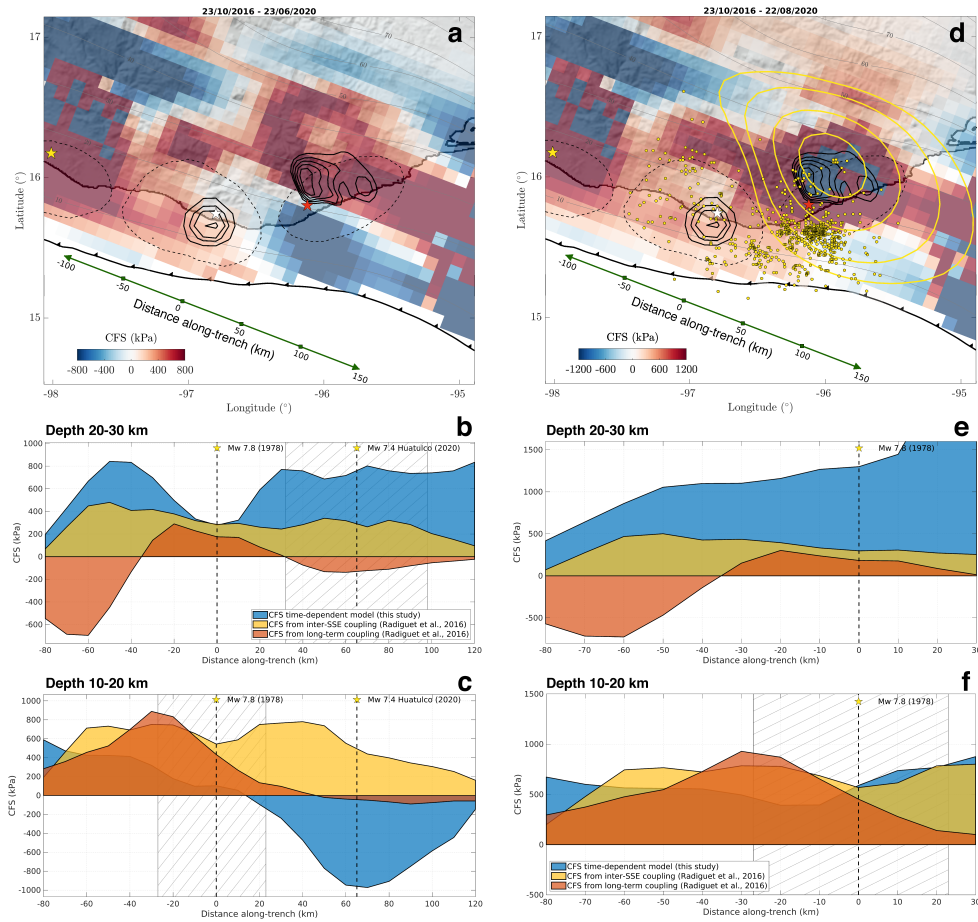


**Figure 7.** Cumulative CFS from the time-variant model and its comparison with the stress built up predicted by time-invariant coupling models. a Cumulative CFS in the plate interface between October 2016 and the date of the 2020 Huatulco earthquake. Black contours represent the isoslip values for the 2020 Huatulco and 1978 Puerto Escondido (Mikumo et al., 2002) earthquakes. Black dashed lines delimit the aftershock areas of historic interplate earthquakes. White dashed circles represent the regions where we analyze the evolution of the interplate slip rate and the CFS shown in figures 6, 7c and 7d. b, c Comparison between our cumulative CFS time-variant model and the CFS predicted by time-invariant coupling models of the region (Radiguet et al., 2016) between October 2016 and the date of the 2020 Huatulco earthquake for two depth bands, between 20-30 km depth and between 10-20 km depth, respectively. d Same than a but including the stress contributions from the coseismic and postseismic phases of the Huatulco earthquake. Yellow contours are the 5,10,20 and 30 cm slip isolines of the two months cumulative afterslip. Yellow dots depict the 50 days aftershocks after the Huatulco Earthquake reported by the SSN. e, f Same as b,c but including the stress contribution from the coseismic and postseismic phases of the Huatulco earthquake focused only in the 1978 rupture segment.

total CFS evolution in both regions (black curves, Regions A and B in Figure 4a) together with the linear predictions given by the time-invariant coupling models of Radiguet et al. (2016) (green lines). To assess which slip regime dominates the stress evolution, we also disaggregated the total CFS into the stress contributions produced by slip regions under coupling (creeping) regime only (yellow curves) and by regions undergoing relaxing slip only (red curves).

In the Huatulco rupture zone (Region A, Fig. S14a) our model shows a sustained growth of the total CFS during more than 3.5 years prior to the rupture, reaching values close to 800 kPa and where 75% of the stress contribution comes from regions in coupling regime. The remaining 25% is mainly associated with the SSE occurred following the 2017 Tehuantepec earthquake. In contrast, the long-term time-invariant model predicts a sustained decrease of CFS that implies a continuous reduction of the earthquake potential. On the other hand, while the inter-SSE time-invariant model predicts a growth of the CFS, the final value is about one fourth of what our model yields. This can also be seen in top view by comparing our estimates of CFS in the hypocentral region at the time of the earthquake (Supplementary Movie S1 and Fig. 7a) with those produced by the time-invariant models (Fig. S13). Since the Huatulco earthquake took place, it seems that our time-evolving slip-rate model and its associated CFS represents a more realistic description of the actual megathrust processes than any of the time-invariant coupling models analyzed here.

Considering the 1978 rupture zone (Region B, Fig. S14b), our model reveals significant temporal variations primarily controlled by the stress contributions from regions under coupling regime. The cumulative stress produced by SSEs at the time of the Huatulco earthquake is about 100 kPa and, therefore, the main responsible for the accumulated positive CFS in this region. For this specific region, both inter-SSE and long-term time-invariant models predict a much higher cumulative stress. When integrating the stress contributions from the coseismic and postseismic slip of the Huatulco earthquake, then our stress estimate becomes similar to the long-term estimation and closer (but still much smaller) to the inter-SSE prediction with CFS values around 700 kPa.

Figures 8a and 8b show separately the regional contributions to the CFS of both the relaxing and the creeping (i.e., under coupling regime) slip, respectively, during the whole analyzed period before the Huatulco earthquake. Although in very different proportions, both stress contributions promote an increase in earthquake potential in the rupture areas of the Huatulco and 1978 earthquakes. Figures 8c and 8d show the percentages of these contributions with respect to the total CFS only where the latter is positive in Figure 7a (i.e., where there is an effective increase of the earthquake potential).

Between 20-30 km depth, where regions A and C are located, we observe that most of the accumulated stress ( $\sim 65\text{-}80\%$ ) was generated by coupled interface regions and the remaining  $\sim 20\text{-}35\%$  by the relaxing slip (i.e., long- and short-term SSEs, and the Pinotepa earthquake afterslip) that occurred in the region during more than 3.5 years (Figs. S13a and S14c). Given its proximity with the Pinotepa earthquake, Region F differs significantly from this stress partitioning because it is strongly affected by the stresses produced during the coseismic slip and afterslip of the event (Fig. S14f).

For shallower depths, offshore Region D, which has no prestress earthquake potential, experienced a sustained reduction of CFS due to both coupling-related stress shadows (Fig. 8a) and short-term SSEs (Fig. 8b) in similar proportions (Fig. S14d). In contrast, although the stress partitioning between them is not very consistent, Regions B and E do show an increase in earthquake potential. In region B (Fig. S14b), due to the high variability of the PIC, the regions in coupling regime produce a stress release there, i.e., a negative stress contribution. However, the total stress accumulation in this region during the analyzed period is positive. This is because the stress produced by the relaxing slip overcame the stress deficit produced by the coupled portions of the interface and, therefore, its contribution is 170% of the final CFS. In region E (Fig. S14e), both stress contributions are very similar,

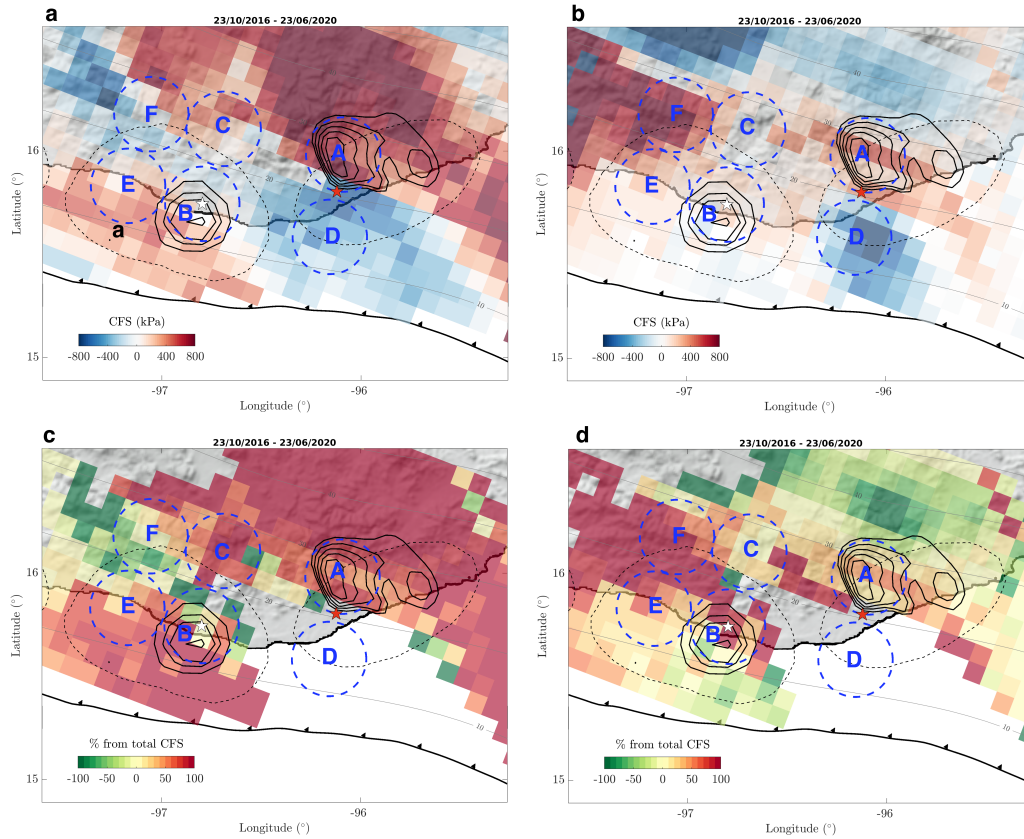


**Figure 8.** CFS contributions by regions in coupling regime and relaxing slip. a and b show the cumulative CFS contributions in the plate interface between October 2016 and the date of the 2020 Huatulco earthquake associated with regions in coupling regime and relaxing slip, respectively. c and d show the CFS contributions (in %) on the plate interface where the total CFS is positive (see figure 7a) by regions in coupling regime and relaxing slip, respectively

494 with 45% due to regions under coupling regime and the other 55% associated with relaxing  
 495 slip. These estimations show the highly heterogeneous stress accumulation and partitioning  
 496 along the plate interface in the Oaxaca segment.

## 497 5 Discussion

498 Previous M7 class interplate earthquakes such as those of 1965 and 1928 occurred in  
 499 close proximity of the 2020 Huatulco rupture, suggesting a possible reactivation of the same  
 500 asperity over time (Chael & Stewart, 1982; Singh et al., 1984). Historical data also suggest  
 501 that two older, probably thrust earthquakes with magnitude larger than 7 occurred nearby  
 502 in 1870 and 1801 (Suárez et al., 2020). Assuming that all these events broke the same plate  
 503 interface patch, their average return period would be 55 +/- 13 years.

504 In this Oaxaca region, the great Mw ~8.6 San Sixto earthquake ruptured a ~300 km  
 505 along-strike segment in 1787 producing a very large tsunami offshore Oaxaca (Suárez &  
 506 Albini, 2009; Ramírez-Herrera et al., 2020). Such event must have involved several locked  
 507 segments along the Oaxaca megathrust, including offshore shallow portions of the plate  
 508 interface to generate the mega-tsunami. Whether M8+ events may repeat depends, among  
 509 other factors, on the interplate mechanical properties and constructive stress interaction  
 510 between different locked and unlocked fault segments (Kaneko et al., 2010, 2018), which  
 511 evolve with time and may escape from the quantitative analysis of known seismicity over  
 512 the last century (Nocquet et al., 2017). Recent laboratory experiments and theoretical fault  
 513 models strongly suggest that friction is a very sensitive function of the interplate slip velocity  
 514 where SSEs take place (Im et al., 2020). Therefore, since the slip velocity changes over time,  
 515 as shown in this study, such variations should play an important role in the dynamic stability  
 516 of the megathrust because of both their frictional counterparts and the associated stress  
 517 changes documented here for the Oaxaca subduction zone. To have an insight into the  
 518 actual megathrust earthquake potential (i.e., to assess whether adjacent locked segments  
 519 are likely to break jointly to produce a much larger event) it is thus necessary a proper  
 520 and continuous quantification of the stress accumulation as proposed here. Monitoring  
 521 the interplate slip-rate continuously might also allow us to constrain the evolution of the  
 522 frictional parameters that control the slip stability conditions on the megathrust.

523 An interesting feature of the Huatulco earthquake is that rupture did not propagate into  
 524 the adjacent updip segment (above ~17 km depth). Impeding rupture into this shallower  
 525 segment might be partly explained with the existence of the large stress barrier produced  
 526 by both the stress shadow from nearby strongly coupled zones and persistent short-term  
 527 SSEs updip (i.e., offshore, see Figures 4b and 7a). However, other factors such as the  
 528 geometry of the interface (e.g. subducted plate reliefs in the region, as recently proposed in  
 529 the Guerrero seismic gap (Plata-Martínez et al., 2021)) and frictional variations could also  
 530 contribute to the explanation of this particular rupture pattern. The spatial concentration  
 531 of aftershocks during the first 50 days following the Huatulco event is clearly shifted updip  
 532 (about 30 km) from the rupture area, where the afterslip developed and the CFS strongly  
 533 increased (Fig. 7d). Only very few aftershocks lie within the main slip patch, indicating an  
 534 effective stress release in most of the rupture area, which is consistent with other M7 class  
 535 earthquakes observed worldwide (Wetzler et al., 2018). Also interesting is the earthquake  
 536 initiation at the shallowest extremity of the rupture zone and its northward propagation.  
 537 The nucleation point lies in the very limit between a highly stressed (downdip) and a highly  
 538 relaxed (updip) interface regions (Fig. 7a), which means on a place with relatively large  
 539 stress gradient and, therefore, deformation. The initiation of the earthquake at this point  
 540 is therefore well explained by our model, as is its propagation towards the most loaded,  
 541 downdip interface region.

542 Our results also suggest that the interplate coupling in Oaxaca is variable in space and  
 543 time (Figs. 5, S11 and S12). Such remarkable PIC variations might certainly be associated  
 544 with changes in the mechanical properties of the fault zone materials induced by the dynamic

545 perturbations of seismic waves from recent significant regional earthquakes (Cruz-Atienza  
 546 et al., 2021; Materna et al., 2019; Delorey et al., 2015). However, PIC variations in the  
 547 shallow, seismogenic zone (i.e., between 10 and 20 km depth) are also somehow linked to  
 548 the occurrence of long-term deeper SSEs (Figs. 5b and S12c). To explain these variations  
 549 at shallow depths we favor the idea involving transient fluctuations of fluid pressure, as  
 550 proposed for the long-term SSEs in the Guerrero (Cruz-Atienza et al., 2018), southern  
 551 Cascadia (Materna et al., 2019), Japan (Bedford et al., 2020) and Hikurangi (Warren-Smith  
 552 et al., 2019) subduction zones. Recent models evoking the fault-valving concept show that  
 553 overpressure fluid pulses migrate upward as the permeability evolves in the fault zone due to  
 554 slow deformation processes (Cruz-Atienza et al., 2018; Shapiro et al., 2018; Zhu et al., 2020).  
 555 These transient changes in pore pressure may lead to large variations of the fault strength as  
 556 high as  $\sim 10\text{-}20$  MPa (Zhu et al., 2020), which makes this mechanism a plausible candidate  
 557 to explain the strong and systematic PIC variations we found in the shallow seismogenic  
 558 zone of Oaxaca during the occurrence of SSEs.

559 Earthquake potential depends on the state of stress along the subduction zone which,  
 560 as shown here, is a function of different evolving processes taking place from the trench to its  
 561 deep portion, where the mechanical interaction between the plates ceases. The stress build-  
 562 up therefore changes over time and space in a complex way, so does the earthquake potential.  
 563 Time-invariant estimates of the interplate coupling are often used to identify seismogenic  
 564 segments prone to large earthquakes (Chlieh et al., 2008; Loveless & Meade, 2011; Moreno  
 565 et al., 2010; Perfettini et al., 2010). However, while these estimates are certainly useful on  
 566 a large spatial and temporal scale, they do not provide a reliable picture of the earthquake  
 567 potential associated with smaller ( $7 < M < 8.5$ ) but potentially devastating ruptures that  
 568 occur more frequently, as shown in this work for the Oaxaca megathrust.

569 Our results indicate that continuous and systematic monitoring of the interplate slip  
 570 velocity, incorporating simultaneously the stressing (i.e., coupled) and relaxing (i.e., slow,  
 571 coseismic and postseismic) slip regions in a continuum, provides a more reliable recon-  
 572 struction of the short-term stress evolution over the megathrust and, probably also, of the  
 573 long-term evolution, which could provide significant insights into the M8+ earthquake su-  
 574 percycles. Proceeding this way may thus be relevant to evaluate theoretical predictions of  
 575 the interface dynamics, which is our leading approach to understand the underlying physics  
 576 in subduction systems.

## 577 6 Conclusions

578 We analyzed the interplate slip-rate evolution during more than 3.5 years in the Oaxaca  
 579 subduction zone including the pre-seismic, coseismic and post-seismic phases associated  
 580 with the June 23, 2020 Mw 7.4 Huatulco earthquake to understand how the different slip  
 581 processes contribute to the plate-interface stress accumulation in the region. We found  
 582 that the main rupture area of the Huatulco earthquake extends between 20 and 33 km  
 583 depth with two main and compact slip patches, the most prominent north the hypocenter  
 584 and the other close to the coast, east-northeast of the hypocenter. The 2020 SSE that  
 585 occurred before the earthquake did not penetrate the rupture area and was preceded by a  
 586 gradual interface decoupling process at a regional scale, including the maximum SSE slip  
 587 area. During the two months preceding the earthquake, when the 2020 SSE developed,  
 588 the Huatulco earthquake rupture area became fully locked. Our slip inversions indicate  
 589 that the two-month earthquake afterslip overlapped the whole coseismic rupture area and  
 590 propagated both to the trench and downdip to the northwest, where most of aftershocks  
 591 happened and where the 2020 SSE was developing, respectively. During the post-seismic  
 592 phase, the rupture area of the 1978 Puerto Escondido earthquake became and remained  
 593 fully coupled. The interplate slip-rate evolution in Oaxaca during the 3.5 years preceding  
 594 the Huatulco earthquake shows that PIC in the megathrust seismogenic region is highly  
 595 variable in time and space. One prominent feature of such variations is a clear correlation  
 596 between PIC increments at shallow depths (10-20 km, including the 1978 rupture area) and

597 the occurrence of three successive SSEs far downdip, suggesting a physical interaction likely  
 598 related to fluid diffusion at the interface, between aseismic slip processes in nearby regions  
 599 that simultaneously relax and load the plate interface.

600 We also found that both relaxing aseismic slip events and megathrust coupling changes  
 601 during those 3.5 years produced a high stress concentration ( $\sim 800$  kPa) over the main as-  
 602 perities of the Huatulco earthquake, as well as a large and shallow (offshore) stress reduction  
 603 ( $\sim 900$  kPa) that may have impeded (along with other possible factors) the updip propa-  
 604 gation of the earthquake. Our results indicate that continuous monitoring of the interplate  
 605 aseismic slip-rate and its CFS counterpart provide a better estimation of M7+ earthquake  
 606 potential over seismogenic regions than predictions detached from time-independent inter-  
 607 plate coupling models. Finally, the stress imparted during the coseismic and postseismic  
 608 phases of the Huatulco earthquake on the 1978 Puerto Escondido rupture area (and its  
 609 downdip portion between 20 and 30 km depth) makes it a region prone to the next earth-  
 610 quake in the near future, a prediction that is consistent with the  $\sim 50$  years earthquake  
 611 return period in the Oaxaca region.

## 612 Acknowledgments

613

614 We are grateful for the outstanding technical support of Eduardo Murrieta and Luciano  
 615 Díaz in the maintenance of the Gaia supercomputing platform, and Luis Salazar in the  
 616 TLALOCNet field operations and stations maintenance. We thank Mathilde Radiguet for  
 617 kindly providing us the long-term coupling models. We also thank Shri Krishna Singh,  
 618 Arturo Iglesias and Gerardo Suárez for fruitful discussion; the Servicio Sismológico Nacional  
 619 (SSN), the Servicio Mareográfico Nacional (SMN) and the Servicio de Geodesia Satelital, all  
 620 of them from the Instituto de Geofísica-UNAM, for all GNSS, strong motion and tide gauge  
 621 data, as well as all their personnel for data acquisition and distribution; and the European  
 622 Space Agency for access to the Sentinel1 data. Part of the GPS and strong motion data  
 623 analyzed in this study are available under some restrictions in the repository of the ?Servicio  
 624 Sismológico Nacional de la UNAM? (<http://www.ssn.unam.mx>). Broadband seismic data  
 625 is publicly available in the same repository. The GPS data in the state of Oaxaca are  
 626 available in the repository of the ?TLALOCNet del Instituto de Geofísica de la UNAM?  
 627 (<http://tlalocnet.udg.mx>). This work is partially based on GNSS data belonging also to  
 628 TLALOCNet and services provided by the GAGE Facility, operated by UNAVCO, Inc.,  
 629 with support from the National Science Foundation and the National Aeronautics and Space  
 630 Administration under NSF Cooperative Agreement EAR-1724794. All GNSS data has been  
 631 processed in the Laboratorio de Geodesia Satelital (LaGeos) of the Instituto de Geofísica-  
 632 UNAM. This work was supported by CONACyT grants 6471 and 255308, UNAM-PAPIIT  
 633 grants IN113814, IG100617 and IG100921, JICA-JST SATREPS-UNAM grant 15543611,  
 634 UNAM-DGTIC grant LANCAD-312 and the graduate school scholarships by CONACyT.

## 635 References

- 636 Bartlow, N. M., Miyazaki, S., Bradley, A. M., & Segall, P. (2011). Space-time correlation  
 637 of slip and tremor during the 2009 cascadia slow slip event. *Geophysical Research*  
 638 *Letters*, *38*(18).
- 639 Bedford, J. R., Moreno, M., Deng, Z., Oncken, O., Schurr, B., John, T., . . . Bevis, M. (2020).  
 640 Months-long thousand-kilometre-scale wobbling before great subduction earthquakes.  
 641 *Nature*, *580*(7805), 628–635.
- 642 Beroza, G. C., & Ide, S. (2011). Slow earthquakes and nonvolcanic tremor. *Annual review*  
 643 *of Earth and planetary sciences*, *39*, 271–296.
- 644 Cabral-Cano, E., Pérez-Campos, X., Márquez-Azúa, B., Sergeeva, M., Salazar-Tlaczani, L.,  
 645 DeMets, C., . . . others (2018). Tlalocnet: A continuous gps-met backbone in mexico  
 646 for seismotectonic and atmospheric research. *Seismological Research Letters*, *89*(2A),

373–381.

647  
648  
649  
650  
651  
652  
653  
654  
655  
656  
657  
658  
659  
660  
661  
662  
663  
664  
665  
666  
667  
668  
669  
670  
671  
672  
673  
674  
675  
676  
677  
678  
679  
680  
681  
682  
683  
684  
685  
686  
687  
688  
689  
690  
691  
692  
693  
694  
695  
696  
697  
698  
699  
700  
701

- Chael, E. P., & Stewart, G. S. (1982). Recent large earthquakes along the middle american trench and their implications for the subduction process. *Journal of Geophysical Research: Solid Earth*, *87*(B1), 329–338.
- Chlieh, M., Avouac, J.-P., Sieh, K., Natawidjaja, D. H., & Galetzka, J. (2008). Heterogeneous coupling of the sumatran megathrust constrained by geodetic and paleogeodetic measurements. *Journal of Geophysical Research: Solid Earth*, *113*(B5).
- Correa-Mora, F., DeMets, C., Cabral-Cano, E., Marquez-Azua, B., & Diaz-Molina, O. (2008). Interplate coupling and transient slip along the subduction interface beneath Oaxaca, Mexico. *Geophysical Journal International*, *175*(1), 269–290.
- Cotte, N., Walpersdorf, A., Kostoglodov, V., Vergnolle, M., Santiago, J.-A., & Campillo, M. (2009). Anticipating the next large silent earthquake in Mexico. *Eos, Transactions American Geophysical Union*, *90*(21), 181–182.
- Cruz-Atienza, V. M., Tago, J., Villafuerte, C., Wei, M., Garza-Girón, R., Dominguez, L. A., ... others (2021). Short-term interaction between silent and devastating earthquakes in Mexico. *Nature Communications*, *12*(1), 1–14.
- Cruz-Atienza, V. M., Villafuerte, C., & Bhat, H. S. (2018). Rapid tremor migration and pore-pressure waves in subduction zones. *Nature communications*, *9*(1), 1–13.
- Delorey, A. A., Chao, K., Obara, K., & Johnson, P. A. (2015). Cascading elastic perturbation in Japan due to the 2012 Mw 8.6 Indian Ocean earthquake. *Science Advances*, *1*(9), e1500468.
- DeMets, C., Gordon, R. G., & Argus, D. F. (2010). Geologically current plate motions. *Geophysical Journal International*, *181*(1), 1–80.
- de México Seismology, U. N. A., et al. (2013). Ometepec-pinotepa nacional, Mexico earthquake of 20 March 2012 (Mw 7.5): A preliminary report. *Geofísica Internacional*, *52*(2), 173–196.
- Graham, S., DeMets, C., Cabral-Cano, E., Kostoglodov, V., Rousset, B., Walpersdorf, A., ... Salazar-Tlaczani, L. (2016). Slow slip history for the Mexico subduction zone: 2005 through 2011. In *Geodynamics of the Latin American Pacific Margin* (pp. 3445–3465). Springer.
- Graham, S. E., DeMets, C., Cabral-Cano, E., Kostoglodov, V., Walpersdorf, A., Cotte, N., ... Salazar-Tlaczani, L. (2014a). GPS constraints on the 2011–2012 Oaxaca slow slip event that preceded the 2012 March 20 Ometepec earthquake, southern Mexico. *Geophysical Journal International*, *197*(3), 1593–1607.
- Graham, S. E., DeMets, C., Cabral-Cano, E., Kostoglodov, V., Walpersdorf, A., Cotte, N., ... Salazar-Tlaczani, L. (2014b). GPS constraints on the Mw = 7.5 Ometepec earthquake sequence, southern Mexico: Coseismic and post-seismic deformation. *Geophysical Journal International*, *199*(1), 200–218.
- Gualandi, A., Perfettini, H., Radiguet, M., Cotte, N., & Kostoglodov, V. (2017). GPS deformation related to the Mw 7.3, 2014, Papanao earthquake (Mexico) reveals the aseismic behavior of the Guerrero seismic gap. *Geophysical Research Letters*, *44*(12), 6039–6047.
- Heki, K., & Mitsui, Y. (2013). Accelerated Pacific plate subduction following interplate thrust earthquakes at the Japan trench. *Earth and Planetary Science Letters*, *363*, 44–49.
- Hirose, H., Matsuzawa, T., Kimura, T., & Kimura, H. (2014). The Boso slow slip events in 2007 and 2011 as a driving process for the accompanying earthquake swarm. *Geophysical Research Letters*, *41*(8), 2778–2785.
- Im, K., Saffer, D., Marone, C., & Avouac, J.-P. (2020). Slip-rate-dependent friction as a universal mechanism for slow slip events. *Nature Geoscience*, *13*(10), 705–710.
- Kaneko, Y., Avouac, J.-P., & Lapusta, N. (2010). Towards inferring earthquake patterns from geodetic observations of interseismic coupling. *Nature Geoscience*, *3*(5), 363–369.
- Kaneko, Y., Wallace, L. M., Hamling, I. J., & Gerstenberger, M. C. (2018). Simple physical model for the probability of a subduction-zone earthquake following slow slip events

- and earthquakes: Application to the hikurangi megathrust, new zealand. *Geophysical Research Letters*, *45*(9), 3932–3941.
- Lay, T., & Kanamori, H. (1981). An asperity model of large earthquake sequences. *Earthquake Prediction*.
- Li, Y., Shan, X., Zhu, C., Qiao, X., Zhao, L., & Qu, C. (2020). Geodetic model of the 2018 m w 7.2 pinotepa, mexico, earthquake inferred from insar and gps data. *Bulletin of the Seismological Society of America*, *110*(3), 1115–1124.
- Loveless, J. P., & Meade, B. J. (2011). Spatial correlation of interseismic coupling and coseismic rupture extent of the 2011 mw= 9.0 tohoku-oki earthquake. *Geophysical Research Letters*, *38*(17).
- Materna, K., Bartlow, N., Wech, A., Williams, C., & Bürgmann, R. (2019). Dynamically triggered changes of plate interface coupling in southern cascadia. *Geophysical Research Letters*, *46*(22), 12890–12899.
- Melgar, D., Ruiz-Angulo, A., Pérez-Campos, X., Crowell, B. W., Xu, X., Cabral-Cano, E., ... Rodriguez-Abreu, L. (2021). Energetic rupture and tsunamigenesis during the 2020 m w 7.4 la crucecita, mexico earthquake. *Seismological Society of America*, *92*(1), 140–150.
- Melnick, D., Moreno, M., Quinteros, J., Baez, J. C., Deng, Z., Li, S., & Oncken, O. (2017). The super-interseismic phase of the megathrust earthquake cycle in chile. *Geophysical Research Letters*, *44*(2), 784–791.
- Mikumo, T., Yagi, Y., Singh, S. K., & Santoyo, M. A. (2002). Coseismic and postseismic stress changes in a subducting plate: Possible stress interactions between large interplate thrust and intraplate normal-faulting earthquakes. *Journal of Geophysical Research: Solid Earth*, *107*(B1), ESE-5.
- Moreno, M., Melnick, D., Rosenau, M., Bolte, J., Klotz, J., Echtler, H., ... others (2011). Heterogeneous plate locking in the south–central chile subduction zone: Building up the next great earthquake. *Earth and Planetary Science Letters*, *305*(3-4), 413–424.
- Moreno, M., Rosenau, M., & Oncken, O. (2010). 2010 maule earthquake slip correlates with pre-seismic locking of andean subduction zone. *Nature*, *467*(7312), 198–202.
- Nikkhoo, M., & Walter, T. R. (2015). Triangular dislocation: an analytical, artefact-free solution. *Geophysical Journal International*, *201*(2), 1119–1141.
- Nocquet, J.-M., Jarrin, P., Vallée, M., Mothes, P., Grandin, R., Rolandone, F., ... others (2017). Supercycle at the ecuadorian subduction zone revealed after the 2016 pedernales earthquake. *Nature Geoscience*, *10*(2), 145–149.
- Obara, K., & Kato, A. (2016). Connecting slow earthquakes to huge earthquakes. *Science*, *353*(6296), 253–257.
- Perfettini, H., Avouac, J.-P., Tavera, H., Kositsky, A., Nocquet, J.-M., Bondoux, F., ... others (2010). Seismic and aseismic slip on the central peru megathrust. *Nature*, *465*(7294), 78–81.
- Plata-Martínez, R., Ide, S., Shinohara, M., Mortel, E. S. G., Mizuno, N., Ramirez, L. A. D., ... Yamada, T. (2021). Shallow slow earthquakes to decipher future catastrophic earthquakes in the guerrero seismic gap. *Accepted at Nature Communications*.
- Radiguet, M., Cotton, F., Vergnolle, M., Campillo, M., Valette, B., Kostoglodov, V., & Cotte, N. (2011). Spatial and temporal evolution of a long term slow slip event: the 2006 guerrero slow slip event. *Geophysical Journal International*, *184*(2), 816–828.
- Radiguet, M., Perfettini, H., Cotte, N., Gualandi, A., Valette, B., Kostoglodov, V., ... Campillo, M. (2016). Triggering of the 2014 m w 7.3 papanoa earthquake by a slow slip event in guerrero, mexico. *Nature Geoscience*, *9*(11), 829–833.
- Ramírez-Herrera, M.-T., Corona, N., Cerny, J., Castillo-Aja, R., Melgar, D., Lagos, M., ... others (2020). Sand deposits reveal great earthquakes and tsunamis at mexican pacific coast. *Scientific Reports*, *10*(1), 1–10.
- Rousset, B., Lasserre, C., Cubas, N., Graham, S., Radiguet, M., DeMets, C., ... others (2016). Lateral variations of interplate coupling along the mexican subduction interface: Relationships with long-term morphology and fault zone mechanical properties. *Pure and Applied Geophysics*, *173*(10), 3467–3486.

- 757 Saffer, D. M., & Wallace, L. M. (2015). The frictional, hydrologic, metamorphic and thermal  
758 habitat of shallow slow earthquakes. *Nature Geoscience*.
- 759 Segall, P., & Bradley, A. M. (2012). Slow-slip evolves into megathrust earthquakes in 2d  
760 numerical simulations. *Geophysical Research Letters*, *39*(18).
- 761 Shapiro, N. M., Campillo, M., Kaminski, E., Vilotte, J.-P., & Jaupart, C. (2018). Low-  
762 frequency earthquakes and pore pressure transients in subduction zones. *Geophysical  
763 Research Letters*, *45*(20), 11–083.
- 764 Singh, S., Astiz, L., & Havskov, J. (1981). Seismic gaps and recurrence periods of large  
765 earthquakes along the mexican subduction zone: A reexamination. *Bulletin of the  
766 seismological Society of America*, *71*(3), 827–843.
- 767 Singh, S., Dominguez, T., Castro, R., & Rodriguez, M. (1984). P waveform of large, shallow  
768 earthquakes along the mexican subduction zone. bulletin of the seismological society  
769 of america. *Bulletin of the seismological Society of America*, *74*(6), 2135–2156.
- 770 Suárez, G., & Albini, P. (2009). Evidence for great tsunamigenic earthquakes (m 8.6)  
771 along the mexican subduction zone. *Bulletin of the Seismological Society of America*,  
772 *99*(2A), 892–896.
- 773 Suárez, G., Ruiz-Barón, D., Chico-Hernández, C., & Zúñiga, F. R. (2020). Catalog of  
774 preinstrumental earthquakes in central mexico: epicentral and magnitude estimations  
775 based on macroseismic data. *Bulletin of the Seismological Society of America*, *110*(6),  
776 3021–3036.
- 777 Suárez, G., Santoyo, M. A., Hjorleifsdottir, V., Iglesias, A., Villafuerte, C., & Cruz-Atienza,  
778 V. M. (2019). Large scale lithospheric detachment of the downgoing cocos plate: The  
779 8 september 2017 earthquake (mw 8.2). *Earth and Planetary Science Letters*, *509*,  
780 9–14.
- 781 Tago, J., Cruz-Atienza, V. M., Villafuerte, C., Nishimura, T., Kostoglodov, V., Real, J.,  
782 & Ito, Y. (2021). Adjoint slip inversion under a constrained optimization frame-  
783 work: Revisiting the 2006 guerrero slow slip event. *Accepted at Geophysical Journal  
784 International*.
- 785 Uchida, N., Iinuma, T., Nadeau, R. M., Bürgmann, R., & Hino, R. (2016). Periodic slow  
786 slip triggers megathrust zone earthquakes in northeastern japan. *Science*, *351*(6272),  
787 488–492.
- 788 Voss, N., Dixon, T. H., Liu, Z., Malservisi, R., Protti, M., & Schwartz, S. (2018). Do slow  
789 slip events trigger large and great megathrust earthquakes? *Science advances*, *4*(10),  
790 eaat8472.
- 791 Warren-Smith, E., Fry, B., Wallace, L., Chon, E., Henrys, S., Sheehan, A., . . . Lebedev, S.  
792 (2019). Episodic stress and fluid pressure cycling in subducting oceanic crust during  
793 slow slip. *Nature Geoscience*, *12*(6), 475–481.
- 794 Wetzler, N., Lay, T., Brodsky, E. E., & Kanamori, H. (2018). Systematic deficiency of after-  
795 shocks in areas of high coseismic slip for large subduction zone earthquakes. *Science  
796 advances*, *4*(2), eaao3225.
- 797 Zhu, W., Allison, K. L., Dunham, E. M., & Yang, Y. (2020). Fault valving and pore  
798 pressure evolution in simulations of earthquake sequences and aseismic slip. *Nature  
799 communications*, *11*(1), 1–11.

*AGU Advances*

Supporting Information for:

**Slow slip events and megathrust coupling changes reveal the earthquake potential  
before the 2020 Mw 7.4 Huatulco, Mexico event**

**Authors:** Carlos Villafuerte<sup>1\*</sup>, V. M. Cruz-Atienza<sup>2</sup>, J. Tago<sup>3</sup>, D. Solano-Rojas<sup>3</sup>,  
R. Garza-Girón<sup>4</sup>, S. I. Franco<sup>2</sup>, L. A. Dominguez<sup>5</sup> and V. Kostoglodov<sup>2</sup>.

<sup>1</sup>Posgrado en Ciencias de la Tierra, Instituto de Geofísica, Universidad Nacional Autónoma de México, Mexico City, Mexico.

<sup>2</sup>Instituto de Geofísica, Universidad Nacional Autónoma de México, Mexico City, Mexico.

<sup>3</sup>Facultad de Ingeniería, Universidad Nacional Autónoma de México, Mexico City, Mexico.

<sup>4</sup>Department of Earth and Planetary Sciences, University of California, Santa Cruz, USA.

<sup>5</sup>Escuela Nacional de Estudios Superiores, Campus Morelia, Universidad Nacional Autónoma de México, Mexico.

\*Correspondence to: [villafuerte.cd@gmail.com](mailto:villafuerte.cd@gmail.com)

**Contents of this file:**

**Supplementary Text S1-S4**

- S1. GNSS time series processing.
- S2. InSAR images processing.
- S3. Slip inversion method.
- S4. Coulomb Failure Stress estimation.

**Supplementary Figures S1-S14**

**Caption of Supplementary Movie S1**

### **Text S1. GNSS time series processing**

The GNSS displacement times series are estimated using the GIPSY 6.4 software package (Lagler et al., 2013), which follows a Precise Point Positioning strategy. The station positions are defined in the International Terrestrial Reference Frame, year 2014 (ITRF 2014). For daily processing we used the Jet Propulsion Laboratory final and non-fiducial products (orbits and clocks). We generated observables using 2 model categories: (1) Earth models and (2) observation models. The Earth models include tidal effects (i.e., solid tides, ocean loading and tide created by polar motion), Earth rotation (UT1), polar motion, nutation and precession. Observation models, on the other hand, are related with phase center offsets, tropospheric effects and timing errors (i.e., relativistic effects). The troposphere delay is estimated like as random walk process. This effect is broken into wet and dry components. The azimuthal gradient and the dry component are estimated using GPT2 model and mapping function (TGIPSY1). The antennas phase center variations are considered through antenna calibration files. For receiver antennas, the correction is estimated taking the International GNSS Service (IGS) Antex file. We also applied a wide-lane phase bias to account for the ambiguity resolution.

To remove the outliers and then estimate the displacement vectors per time window, we first determine the data variance for each component and time window from the differences between daily displacement values and a moving, locally weighted LOESS function (i.e., 2nd order polynomial regressions with a half-window time support, Figs. 2a, 3a and S6). Then, all data points in a time window with differences larger than two standard deviations were

dismissed. Once the outliers are removed, a new regression is performed to estimate the final displacement vectors.

### 1.1 Correction of seasonal effects

To properly associate the displacement time series with the deformation produced by slip processes on the plate interface its necessary to identify and remove the signals associated with seasonal oscillations. We assume that these signals can be modeled as a linear combination of two annual and two semi-annual trigonometric terms excluding inter-annual variations (Bevis and Brown, 2014):

$$S(t_i) = b_1 \sin(2\pi t_i) + b_2 \cos(2\pi t_i) + c_1 \sin(4\pi t_i) + c_2 \cos(4\pi t_i), \quad (1)$$

where  $S(t_i)$  is the seasonal displacement at time  $t_i$  in years units,  $b_1$  and  $b_2$  are the coefficients for the annual terms and  $c_1$  and  $c_2$  the coefficients for the semi-annual terms. We use only inter-SSE time windows of the actual data to identify the contribution of these periodic oscillations to the observed displacements. Thus, we assume that the GNSS time series during an inter-SSE window can be modeled as the sum of their secular inter-SSE displacement and the seasonal contributions as:

$$U(t_i) = a + vt_i + S(t_i)$$

where  $U(t_i)$  represents the GNSS displacement at time  $t_i$  in years units,  $a$  is the intercept and  $v$  the constant secular velocity in the inter-SSE periods. Removing the seasonal

contribution in Oaxaca is challenging because the amplitude and recurrence of the annual and semi-annual terms are comparable to those of the SSEs in the region (from 1-2 years). Since the seasonal effects are much stronger in the vertical component than in the horizontal components, we first determined the coefficients of equation 1 for the vertical component by means of a simple least squares approach. In many stations the length of the inter-SSE windows is no longer than one year, preventing a reliable seasonal-noise characterization in such restrictive time windows. To overcome this problem, we use as many inter-SSE windows as possible in the longest GNSS time series available per station to obtain both the four coefficients of the seasonal function (i.e., the same coefficients for all inter-SSE windows) and the individual secular contribution per window. The inter-SSE windows were manually selected by excluding those periods where clear SSEs and earthquakes afterslip were present (Fig. S7). Then, the displacement time series for the vertical component during inter-SSE periods can be expressed as

$$U_v(t_i) = \begin{cases} a_1 + v_1 t_i + S_v(t_i) & \text{if } T_1^l < t_i < T_1^u \\ a_2 + v_2 t_i + S_v(t_i) & \text{if } T_2^l < t_i < T_2^u \\ \vdots & \\ a_k + v_k t_i + S_v(t_i) & \text{if } T_k^l < t_i < T_k^u \end{cases}$$

where  $a_k$  and  $v_k$  are the intercept and the constant secular velocity during the  $k$  inter-SSE window, respectively,  $S_v$  is the seasonal function for the vertical component, and  $[T_k^l, T_k^u]$  are the lower- and upper-time limits of the  $k$  inter-SSE window. For the treatment of the horizontal displacement components, where the amplitude of the seasonal noise is usually smaller than that of the transient tectonic deformations, we assumed that the seasonal effects on the three components are all proportional. This is a reasonable hypothesis since most of

these contributions are related to the earth's elastic response due to hydrological processes occurring on the surface (Heki et al., 2020). Therefore, the displacement for every horizontal component in the inter-SSE periods,  $U_h$ , can be represented as

$$U_h(t_i) = \begin{cases} a_1 + v_1 t_i + \alpha_h S_v(t_i) & \text{if } T_1^l < t_i < T_1^u \\ a_2 + v_2 t_i + \alpha_h S_v(t_i) & \text{if } T_2^l < t_i < T_2^u \\ \vdots & \\ a_k + v_k t_i + \alpha_h S_v(t_i) & \text{if } T_k^l < t_i < T_k^u \end{cases}$$

where  $\alpha_h$  is the proportionality factor determined also by means of the multi-window least square method, and  $h$  stands for the north-south or east-west component. We decided to proceed in this way because when determining the seasonal functions independently per component (i.e., by independently applying the procedure described for vertical displacements to all components) we realized that the horizontal SSE signals (consistently found at several stations) were in some cases eliminated by applying the correction. Several examples illustrating our approach are shown in Figure S7.

### **Text S2. InSAR images processing**

We calculate a coseismic interferogram of the Huatulco Earthquake using two single look complex Synthetic Aperture Radar (SAR) scenes acquired by the Sentinel-1 satellites in the Interferometric Wide Swath acquisition mode, ascending pass, track 107 (Fig. S2a). The selected scenes were acquired on June 19<sup>th</sup> and June 25<sup>th</sup>, 2020, which correspond to the pair with the shortest-possible acquisition span (6 days). The pass and track were selected to provide the best-possible coverage of the coseismic signal. We use the processing chain provided in the InSAR Scientific Computing Environment (ISCE) (Rosen et al., 2012) to

calculate the interferometric phase between the two SAR scenes, which includes a coarse coregistration assisted by a digital elevation model (DEM), a coarse interferogram calculation, a fine coregistration, a fine interferogram calculation, and basic phase corrections. Accordingly, we additionally use a 1 arc-second DEM from the Shuttle Radar Topography Mission (Farr et al., 2007) to complete the interferogram formation and topographic phase correction. Subsequently, we filter the interferometric phase using a Goldstein filter (Goldstein & Werner, 1998) to later perform phase unwrapping using SNAPHU (Chen & Zebker, 2000). We finally geocode the unwrapped interferogram, convert it to displacement in meters in line of sight (LOS) geometry and mask out water bodies and areas with spatial coherence lower than 0.4 (Fig. S2b).

Geodetic measurements from GNSS and InSAR have different reference frames, which requires converting one into the other to make a fair comparison of the displacements obtained by each technique. GNSS measurements are referenced in East, North and Up components, whereas satellite InSAR have a pixel-wise reference frame in terms of incidence ( $\theta$ ) and azimuth ( $\alpha$ ) angles, which vary pixel by pixel and define the relative LOS direction towards the SAR satellite. GNSS displacements can be projected onto the satellite's LOS direction following the expression (Hanssen, 2001):

$$GPS_{LOS} = -\sin\left(\alpha - \frac{3\pi}{2}\right) \sin\theta d_e - \cos\left(\alpha - \frac{3\pi}{2}\right) \sin\theta d_n + \cos\theta d_u$$

where  $GPS_{LOS}$  is the projection of the GNSS displacement vector onto the LOS vector, and  $d_e$ ,  $d_n$  and  $d_u$  are the GNSS displacement components in the East, North and Up directions,

respectively. Based on this transformation we adapted the ELADIN inversion method (see next section) so that the Somigliana tensor used to generate the synthetic displacements was projected into the individual LOS unit vectors per InSAR data point to perform the simultaneous GNSS and InSAR data inversion.

### **Text S3. Slip inversion method.**

The ELADIN (ELastostatic ADjoint INversion) method (Tago et al., 2021) solves a constrained optimization problem based on the adjoint elastostatic equations with Tikhonov regularization terms, a von Karman autocorrelation function and a gradient projection method to guarantee physically-consistent slip restrictions. The method simultaneously determines the distribution of PIC and relaxing slip (i.e., SSEs and afterslip) in the plate interface to explain the surface displacements. Its precision matrix, which corresponds to the inverse of the data variance matrix (see Section 1), allows to minimize the effect of data errors (i.e., cumulative processing errors and non-tectonic physical signals) by weighting the observations. For the pre-seismic and post-seismic GNSS inversions (Figs. 2 and 3), the weights are directly based on the data variance matrix per time window and displacement component (i.e., ellipses around the tips of the horizontal displacement vectors in Figures 2 and 3) (Tago et al., 2021).

For the coseismic analysis, where GNSS and InSAR displacements are simultaneously inverted (Figs. 1 and S3c), we first inverted each data set independently. The solution using only GNSS data (Fig. S3a) describes a very simple and concentrated slip patch downdip the hypocenter with a maximum value of 4.2 m and a marginally lower than expected moment magnitude  $M_w$  7.32 with average GNSS data error of  $0.2 \pm 0.2$  cm (Fig. S3a). The resulting

model using only InSAR data (Fig. S3b) describes a more heterogeneous slip distribution with maximum value of 2.5 m and a slightly higher moment magnitude of 7.34 with average InSAR data error of  $0.0 \pm 1.2$  cm (Fig. S3b). To combine both data sets in a single joint inversion, the data weights were determined by trial and error until reaching a satisfactory slip solution (Fig. S3c), with maximum value of 3.4 m and average GNSS and InSAR data errors of  $1.2 \pm 1.0$  cm and  $0.2 \pm 2.1$  cm, respectively. The optimal set of weighting factors are such that all InSAR data (i.e., the 221 LOS displacements, Figs. 1b and S2c) were attributed a value equal to one, while the GNSS data (i.e., 12 displacement components) were attributed according to the epicentral distance of each station as follows. The HUAT and OXUM sites weighed 25, the TNSJ site weighed 15, and the OXPE site weighed 5, with these values being the same in all three components per site.

In these inversions we assumed a von Karman Hurst exponent of 0.75 and restricted the slip component perpendicular to the plate convergence direction to be smaller than 0.6 m (for details see Tago et al., 2021). To determine the optimal von Karman correlation length  $L$  for the coseismic joint inversion, we analyzed the problem resolution by means of several mobile checkerboards (MOC) tests (Tago et al., 2021) for a patch size of 20 km and 2.4 m of slip. Each MOC resolution test implies 64 independent checkerboard inversions. For each test we assumed a different  $L$  ranging between 5 and 15 km. Figure S4 shows the MOC test results for the optimal correlation length  $L = 7$  km, which maximizes the average restitution index (ARI) in the 2020 Huatulco earthquake rupture zone and minimizes the data error. An example of a checkerboard inversion with such parameterization is also show in the figure. Our optimal model parameterization guarantees that the coseismic slip inversion has a

nominal error smaller than 35% (i.e., with restitution indexes higher than 0.65) over most of the recovered rupture area for slip patches with characteristic lengths greater than or equal to 20 km (Fig. S4).

Following Tago et al. (2021) and Cruz-Atienza et al. (2021), to guarantee slip restitution indexes higher than 0.5 in the whole Oaxaca region for slip patch sizes larger than 80 km (Fig. S8), we assumed also a Hurst exponent of 0.75 and the optimal correlation length ( $L$ ) of 40 km (parameters of the von Karman function controlling the inverse-problem regularization) for the pre- and post-seismic slip inversions. Also following these works, the slip rake angle could only vary  $30^\circ$  with respect to the plate convergence direction.

As for the inversion exercise mentioned in the main text with a 3.5 km shallower plate interface to match the relocated hypocentral depth of 17.2 km, the slip model (Fig. S5) significantly improved the data fit (i.e., average errors of  $0.7 \pm 0.6$  cm and  $0.1 \pm 1.4$  cm for GNSS and InSAR data, respectively) while reproducing similar source characteristics to those of our preferred solution (Figs. 1a and S3c). However, it is worth noting some differences: (1) the maximum slip is significantly larger (4.3 m), (2) the moment magnitude is smaller ( $M_w$  7.3) as determined from the 1 m slip contour, and (3) the rupture is more concentrated in the main patch north of the hypocenter, between 18 and 30 km deep. For consistency throughout the manuscript (i.e., to assume the same interface geometry in all presented exercises), we keep the deeper solution shown in Figure 1 for subsequent analysis.

#### **Text S4. Coulomb Failure Stress estimation**

The total static stress change on the plate interface is the sum of the stress contributions from plate interface regions that slip, producing either a stress relaxation of the continental crust (i.e., due to SSEs, coseismic slip and afterslip) or a stress built-up (due to regions in coupling regime that we modeled as backslip (Savage, 1983)). To estimate the stress tensor, following Cruz-Atienza et al. (2021) we discretized the 3D plate interface into triangular subfaults and used the artefact-free triangular dislocation method introduced by Nikkhoo and Walter (2015) for a half-space to compute the Coulomb Failure Stress change ( $\Delta CFS$ ) on the plate interface by assuming a locally-consistent thrust mechanism, so that:

$$\Delta CFS = \Delta\tau + \mu\Delta\sigma_n,$$

where  $\Delta\tau$  represents the change of the shear stress in the direction of the fault slip (assumed to be parallel to the plate convergence direction following DeMets et al. (2010));  $\Delta\sigma_n$  is the change of the fault normal stress (positive for tension); and  $\mu$  is the apparent coefficient of friction assumed to be 0.5.

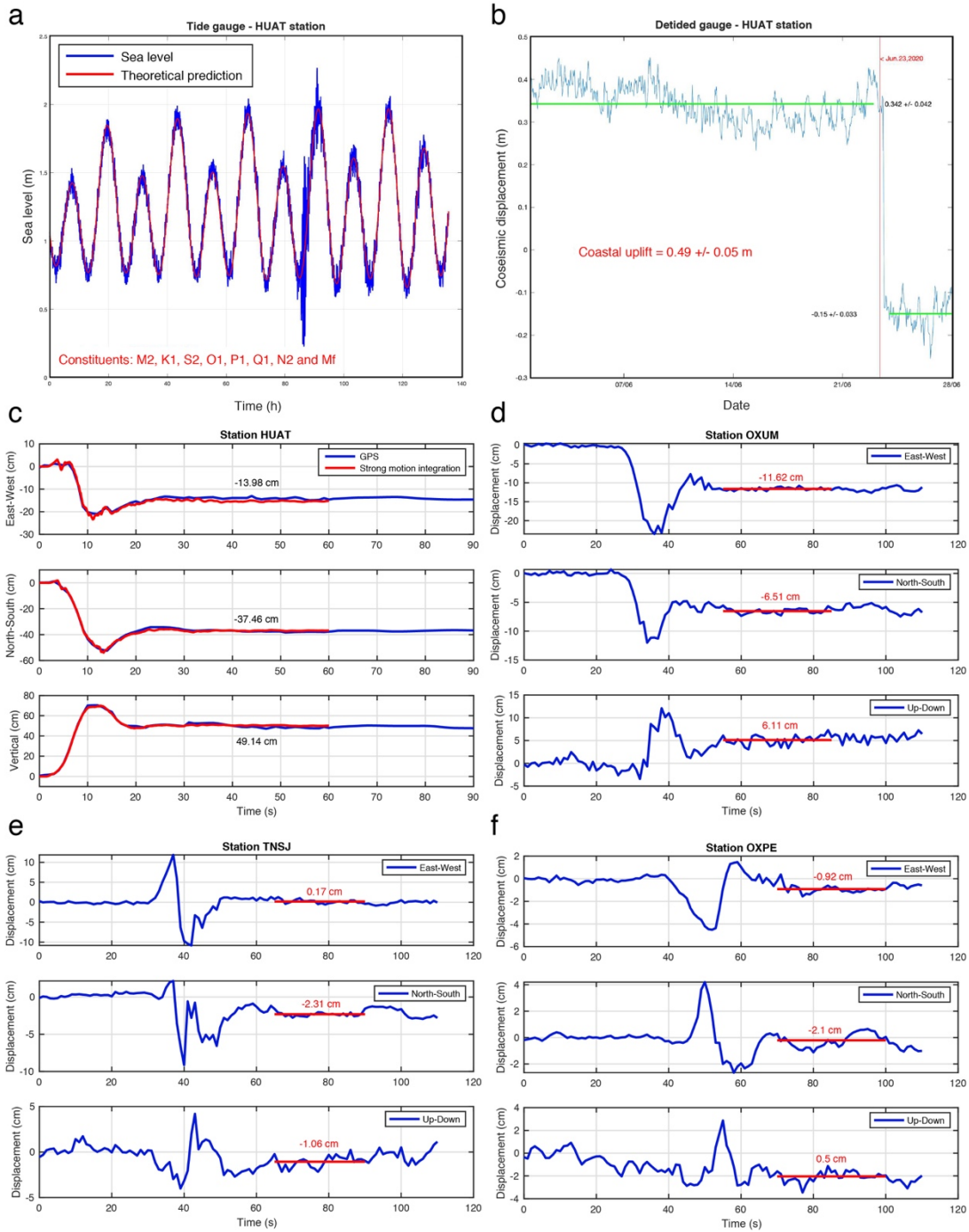


**Figure S1** Huatulco earthquake co-seismic displacements estimated from the HUAT tide gauge (**a** and **b**); high-rate GNSS time series at stations HUAT (**c**), OXUM (**d**), TNSJ (**e**) and OXPE (**f**); and double integration of a strong motion record following the procedure of Wang et al. (2011)(red curve in **c**).

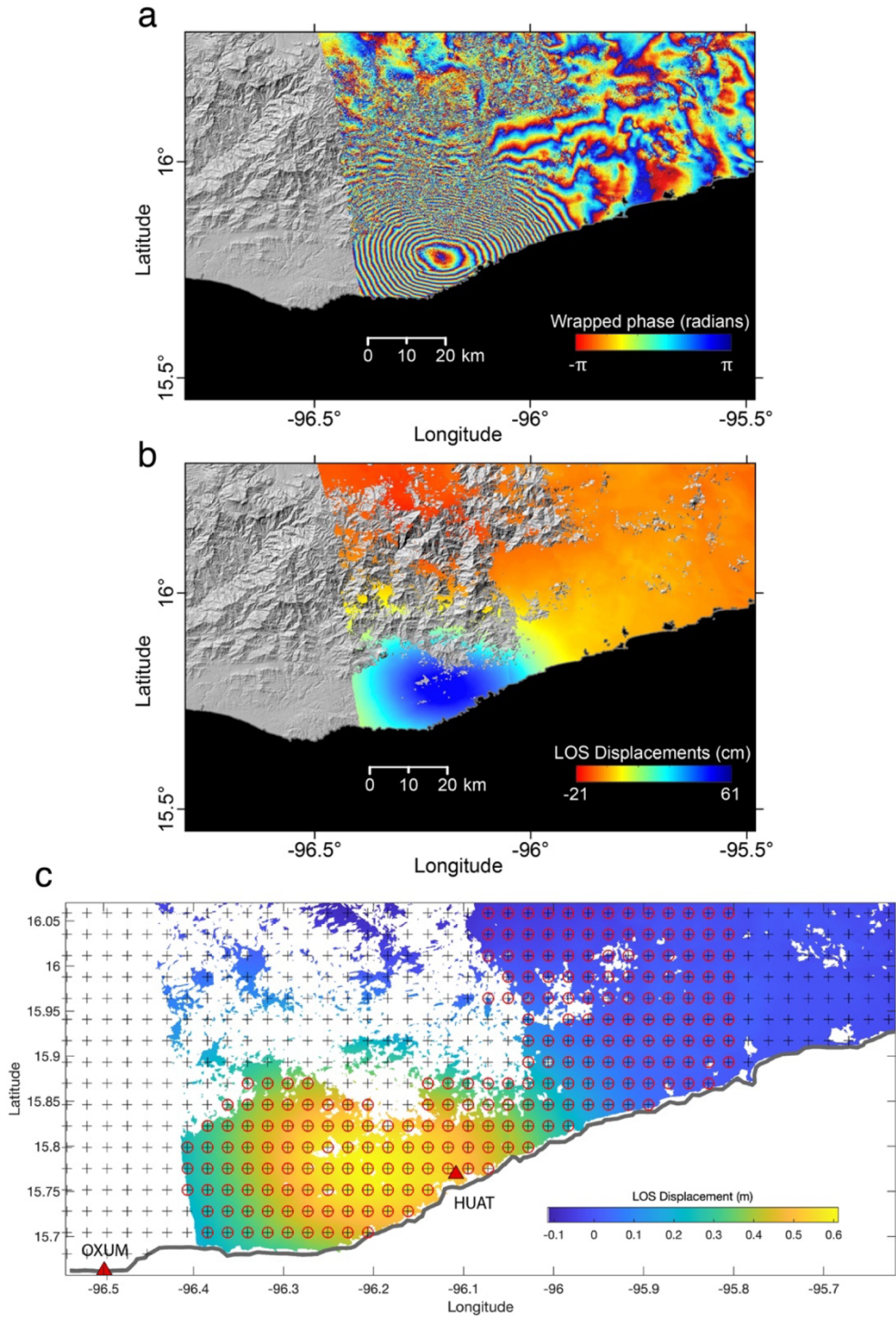


**Figure S2** Huatulco earthquake InSAR displacements estimated from Sentinel satellite images on Track 107 Ascending for scenes on June 19 and 25, 2020. **a** Wrapped phase ascending interferogram. **b** Line of sight (LOS) displacement from ascending track, positive values correspond to motion towards the satellite. **c** Same than **b** but showing the data (circles with crosses) used for the coseismic inversion.

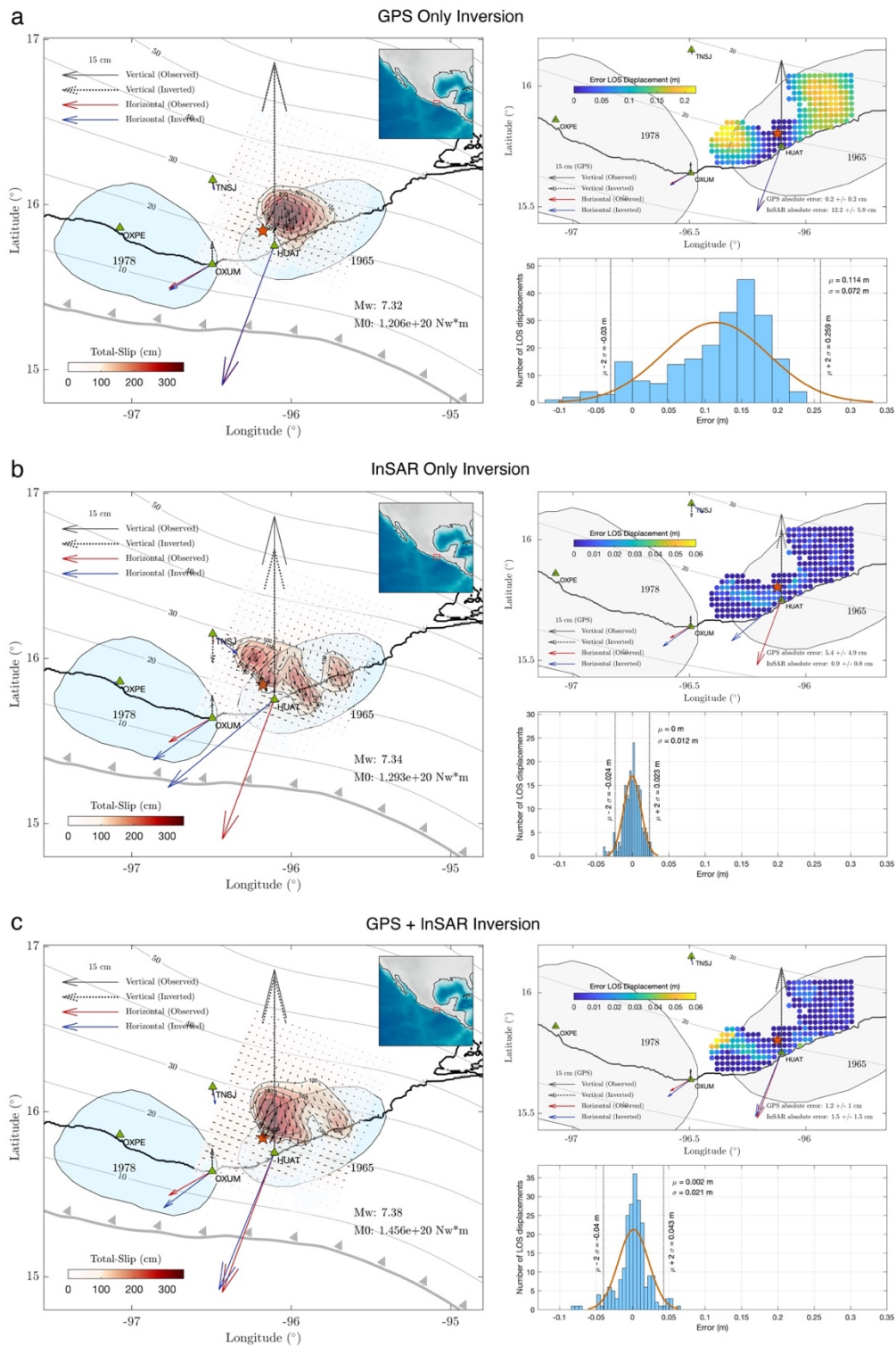


**Figure S3** Coseismic slip inversions for the Huatulco earthquake using different data sets. Coseismic slip inversion (left panel) and their associated misfit GNSS and LOS displacements errors (right panels) using (a) only GNSS data, (b) only InSAR data and (c) both GNSS and InSAR data.

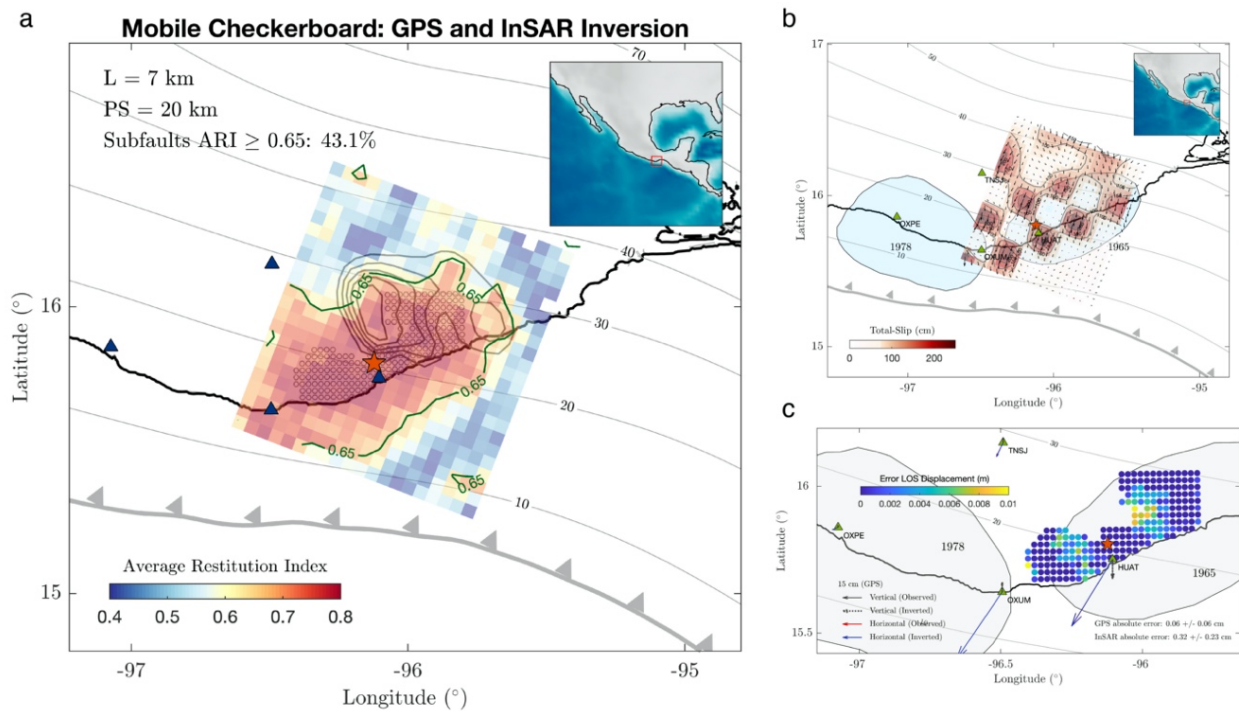


**Figure S4** Resolution analysis for the coseismic GNSS+InSAR joint inversion. **a** Average restitution index (ARI) obtained from a mobile checkerboard (MOC) analysis that integrates 64 independent checkerboard inversions with patch size (PS) of 20 km and correlation length ( $L$ ) of 7 km. Blue triangles are the GNSS stations, small gray circles the InSAR data sites, gray contours our preferred slip model for the 2020 Huatulco earthquake and the red star its epicenter. **b** Example of a single checkerboard slip inversion of the MOC test. **c** GNSS and InSAR displacement errors associated with the checkerboard test shown in **b**.

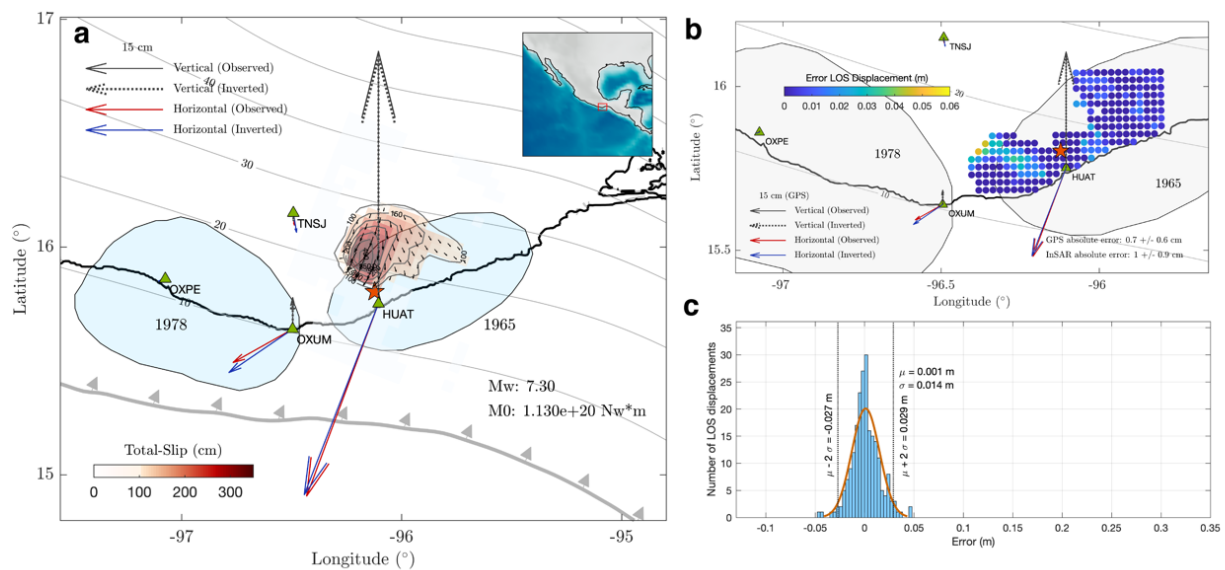


**Figure S5** Huatulco earthquake joint inversion (GNSS and InSAR) assuming that the plate interface has a depth of 17.2 km at the epicenter (i.e., shifted  $\sim 3.5$  km upwards with respect to the interface shown in Figure S3). Coseismic slip inversion (**a**) and their associated misfit GNSS and LOS displacements errors (**b** and **c**).

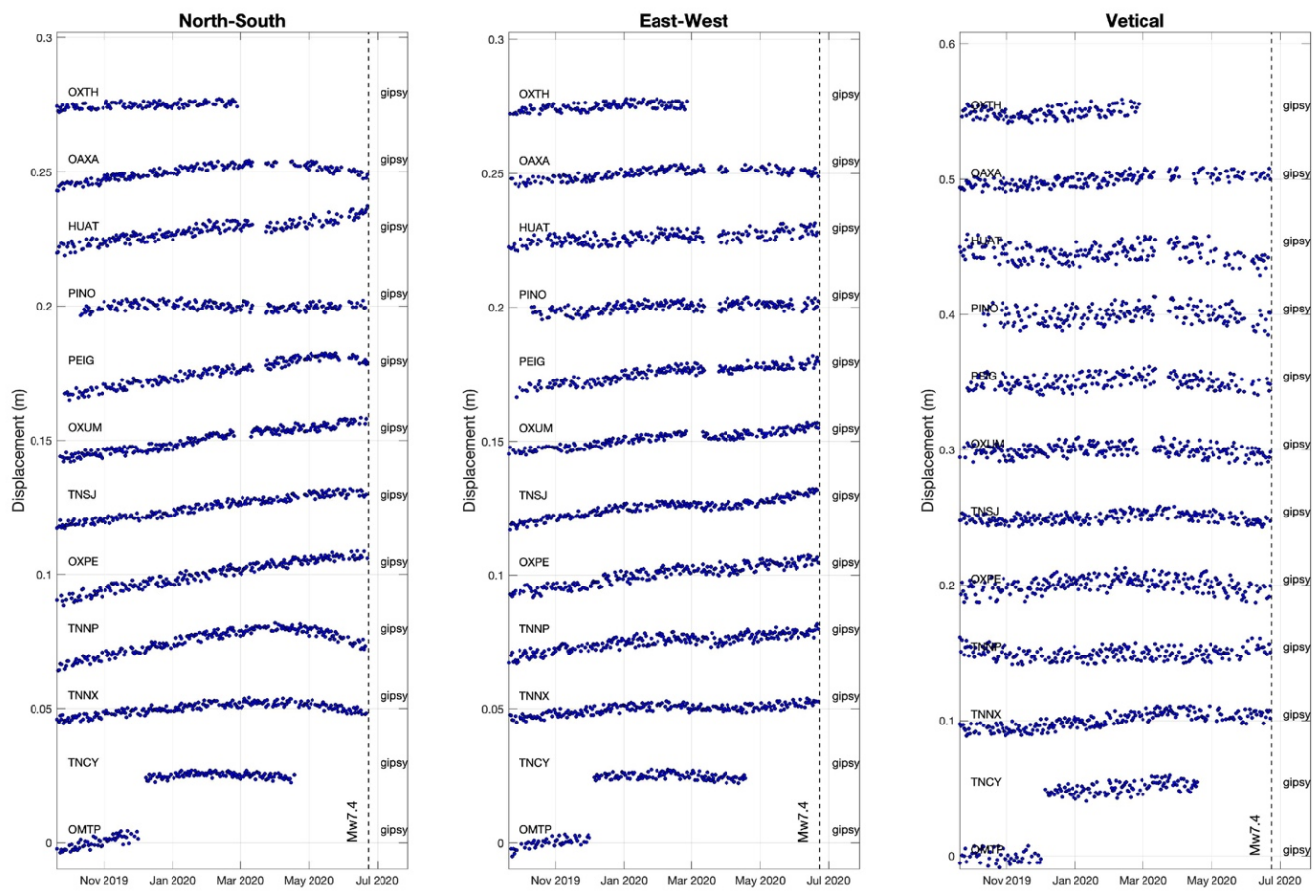


**Figure S6** GNSS displacement time series estimated with the Gipsy-Oasis (v6.4) software for the pre-seismic period in the 12 stations and the three components.

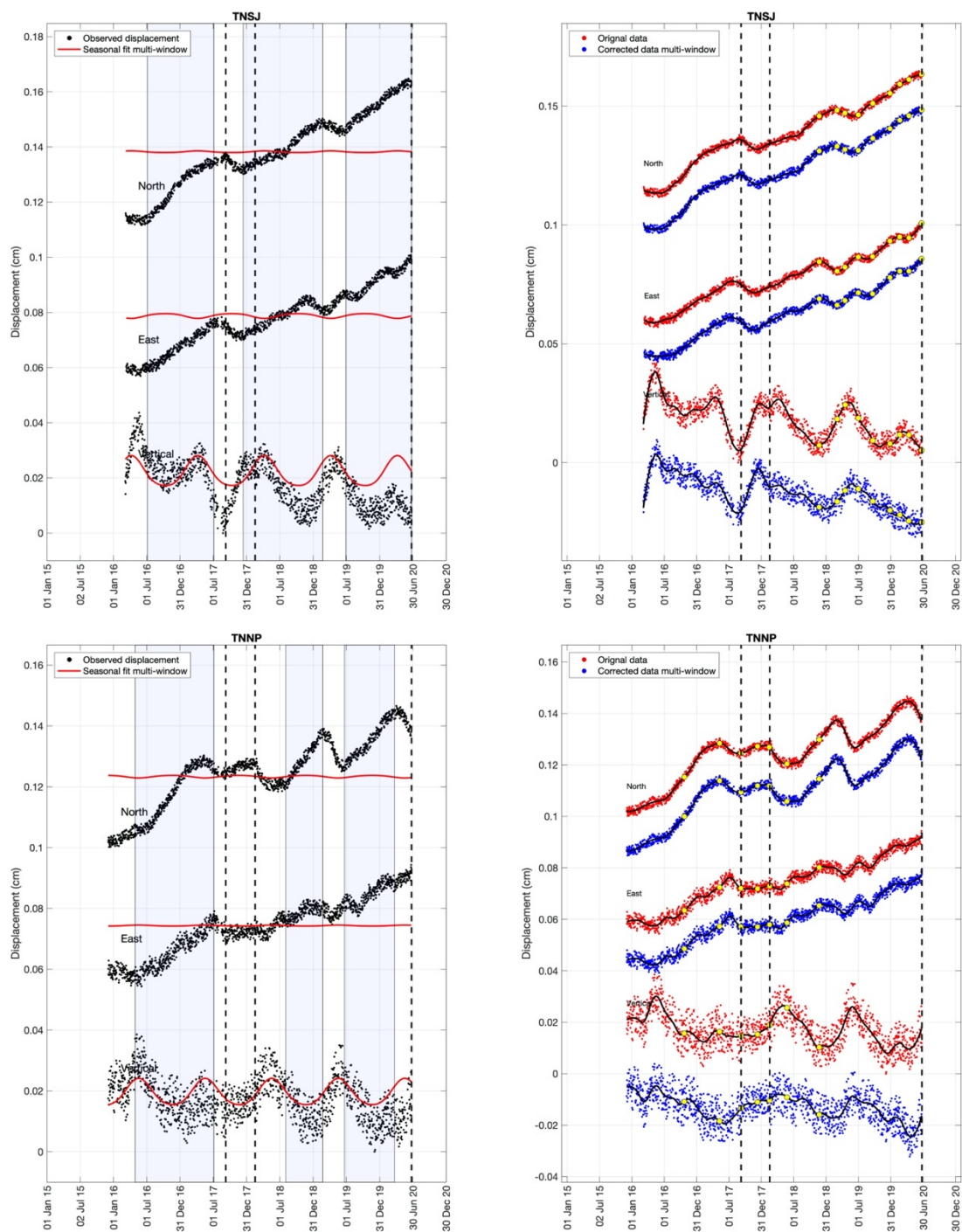


**Figure S7** Example of the correction of displacement time series in station TNSJ for seasonal effects. **a** Pre-processed GNSS time series (black dots) and seasonal functions for every component (red curves) estimated from the multi-window fit procedure. **b** Original (red dots) and corrected (blue dots) displacement time series.

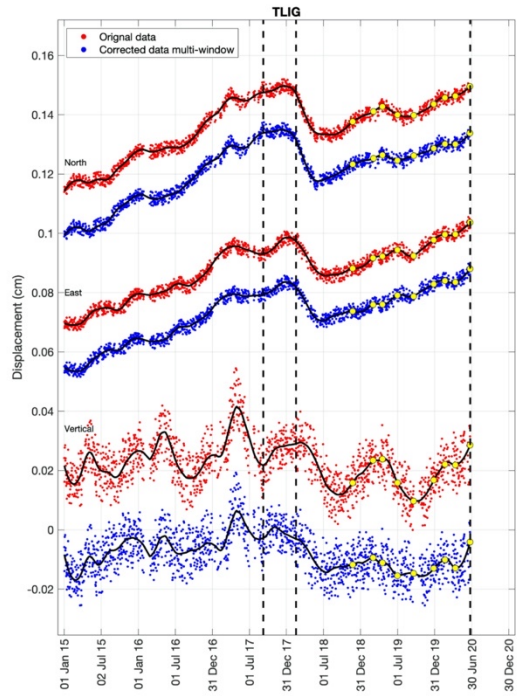
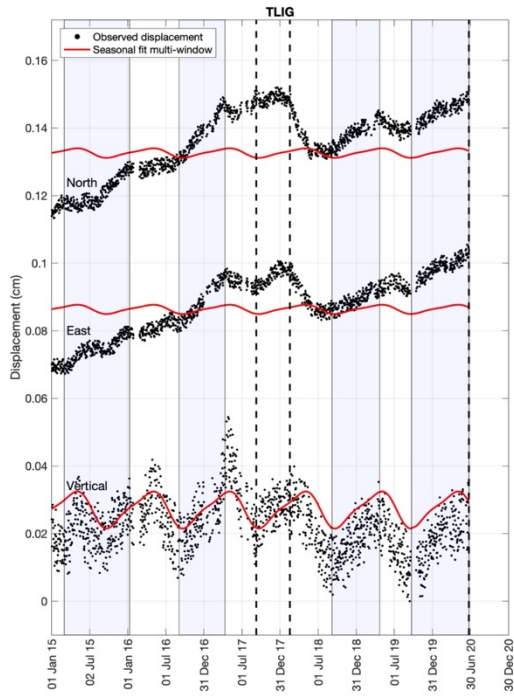
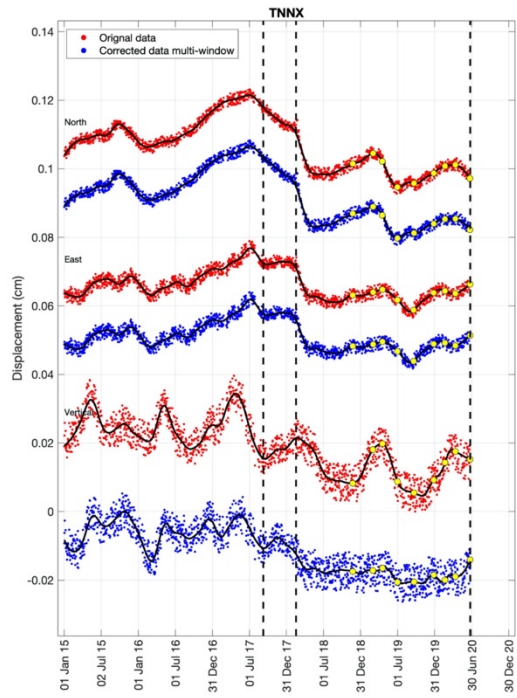
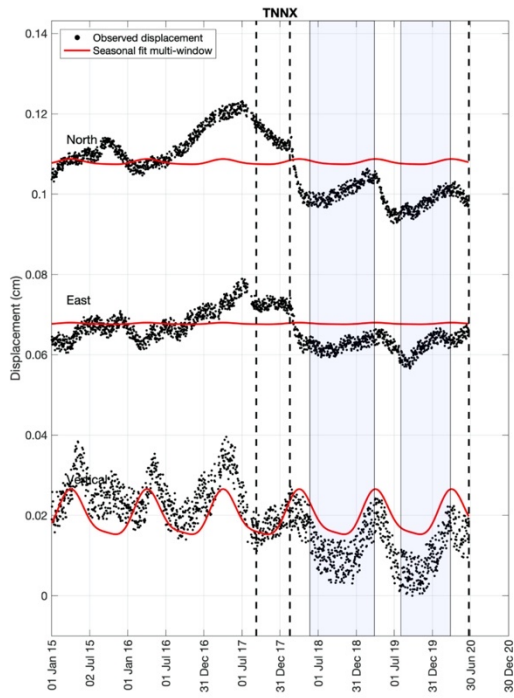
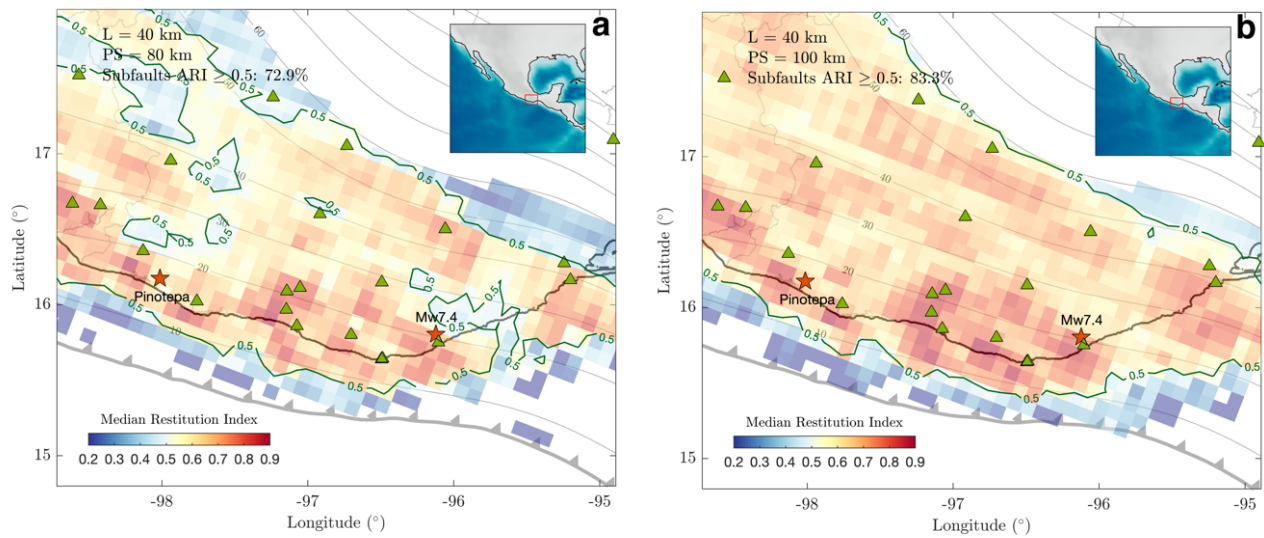
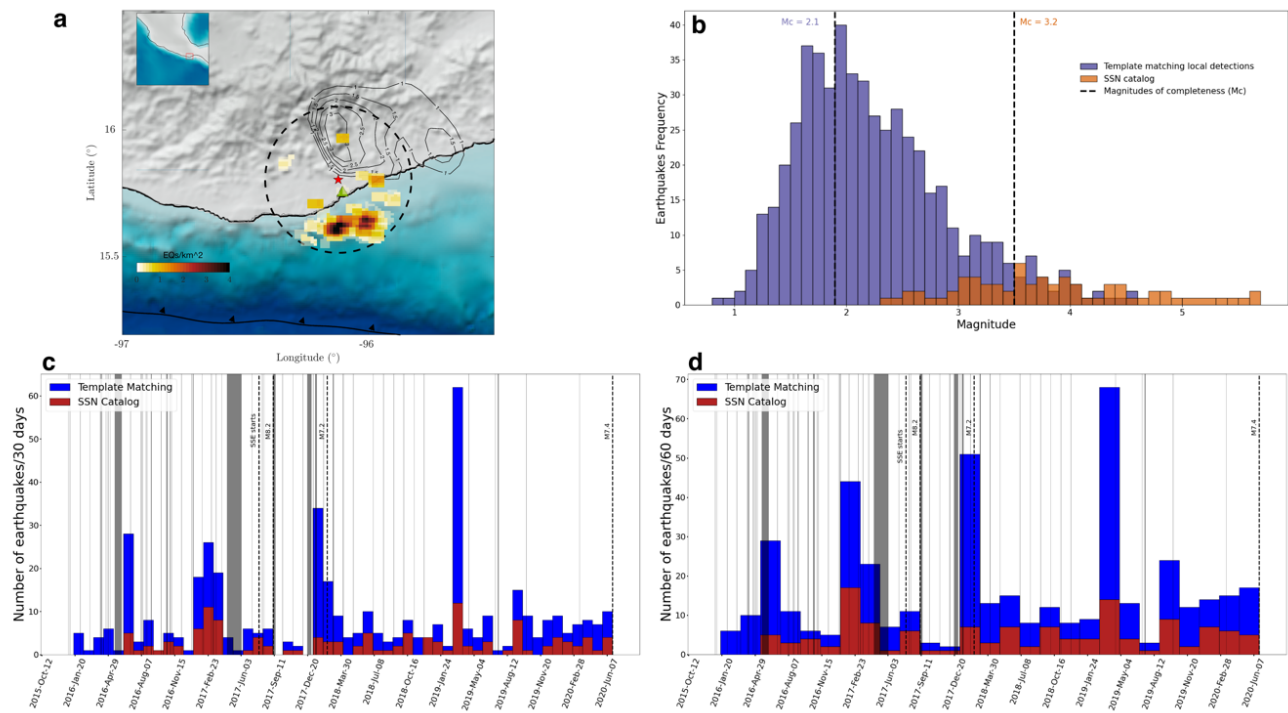


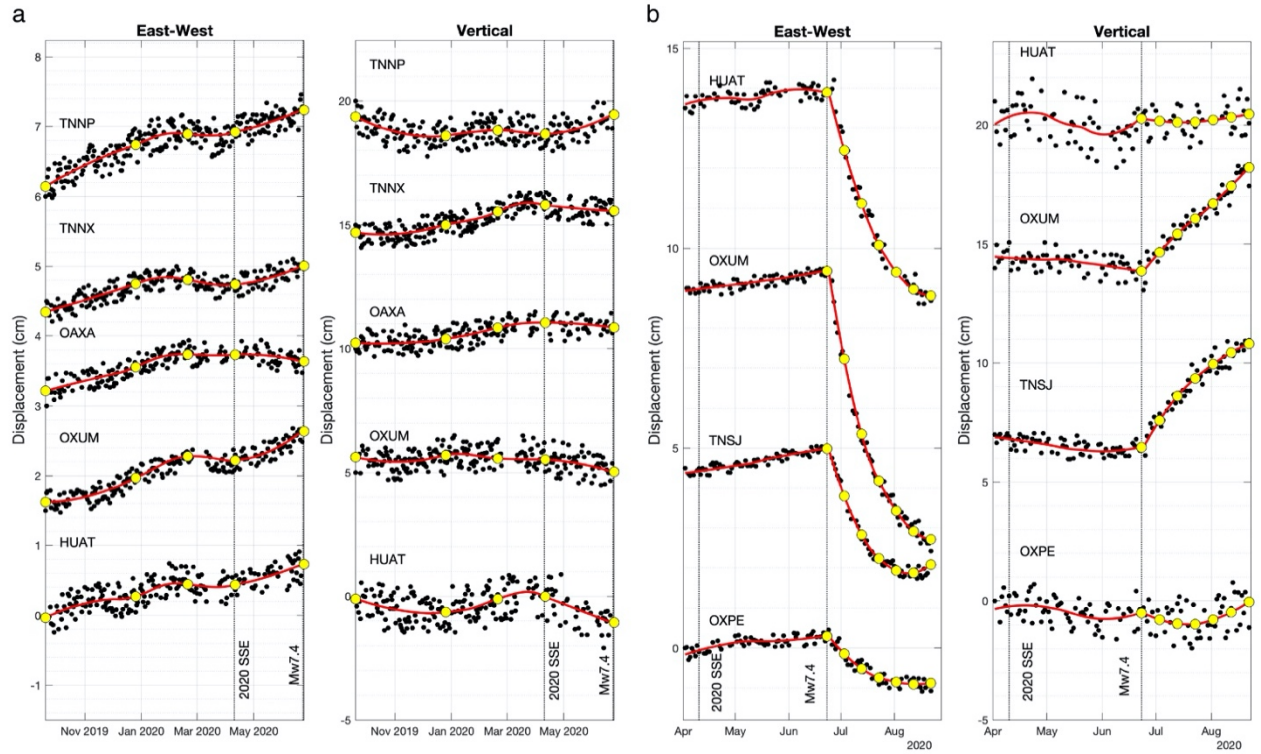
Figure S7 Continuation.



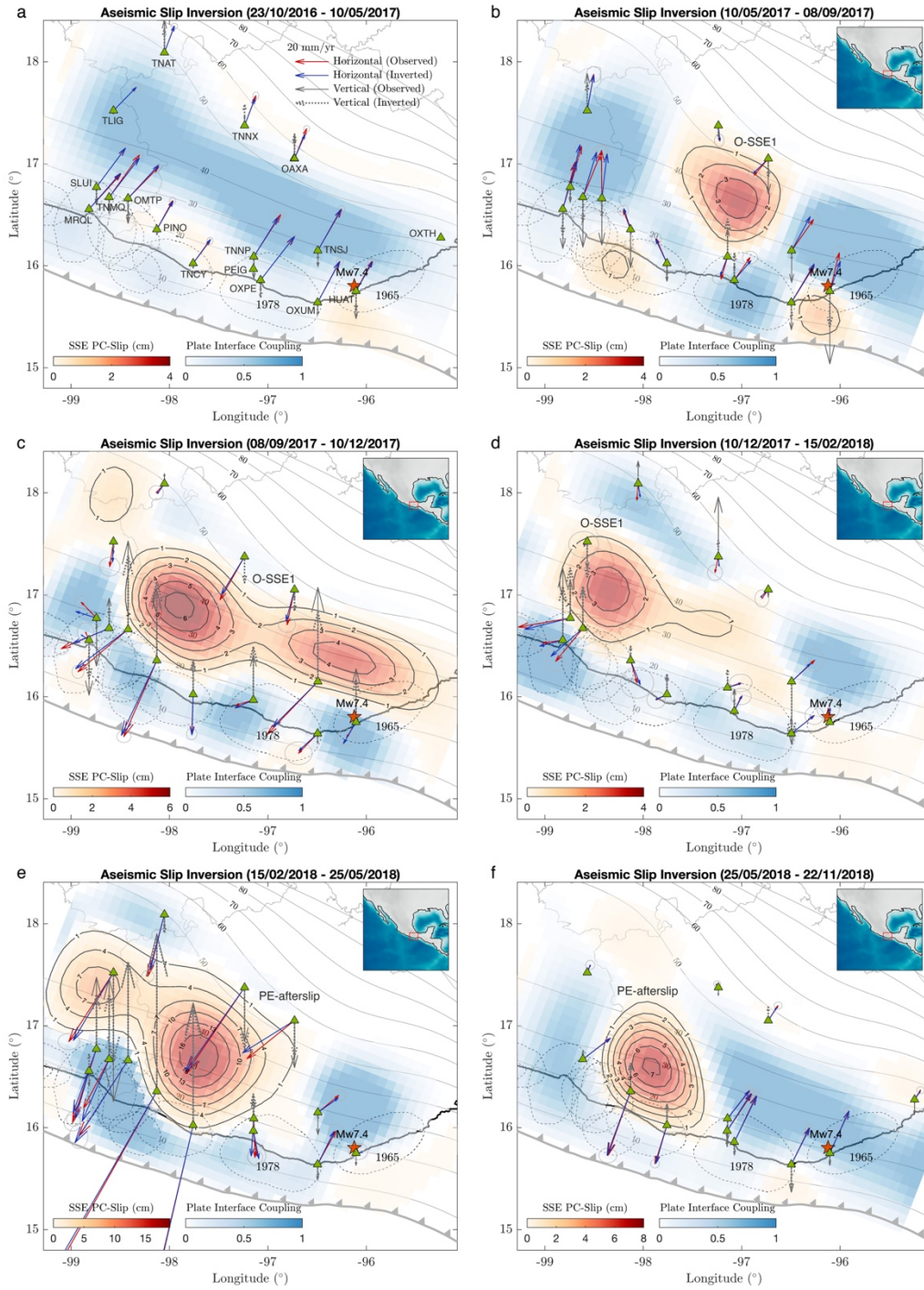
**Figure S8** Resolution analysis for the aseismic slip inversions in Oaxaca. **a** Distribution of the median restitution index obtained from the mobile checkerboard inversion tests considering slip patches sizes of 80 km. **b** Same than a but with slip patches sizes of 100 km. Notice how well resolved are the plate interface regions with depths greater than 10 km.



**Figure S9** Illustration of template matching (TM) results using the one station method (Cruz-Atienza et al., 2020). **a** Density map of precursor TM detections using the closest station HUIG (green triangle) within 30 km from the Huatulco earthquake hypocenter (red star) and  $M > 2.1$ . Notice how almost all the detections are concentrated updip of the hypocenter due to the scarcity of templates located in the Huatulco rupture area. **b** Frequency distributions for the TM and SSN catalogs and their associated magnitude of completeness. **c,d** Seismicity rate evolution for the TM and SSN for two different earthquake rates. Gray sections indicate data gaps.



**Figure S10** East-west and vertical GNSS displacement time series estimated with the Gipsy-Oasis software for the pre-seismic (a) and post-seismic (b) periods in selected stations shown in Figures 2 and 3.



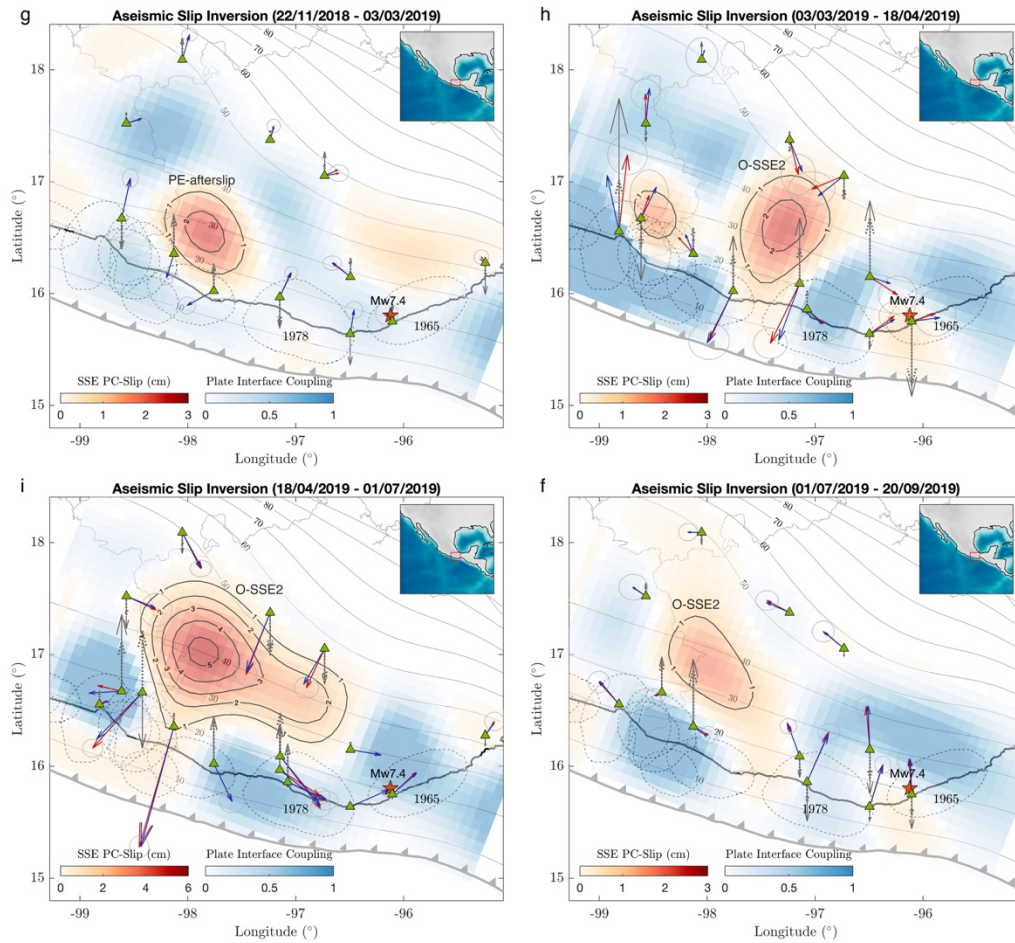


**Figure 11** Detailed evolution aseismic slip inversions in Oaxaca from October 2016 to September 2019 including the 2017 Oaxaca SSE (O-SSE1), the Pinotepa earthquake afterslip (PE-afterslip) and the 2019 Oaxaca SSE (O-SSE2)(see also Supplementary Movie S1).

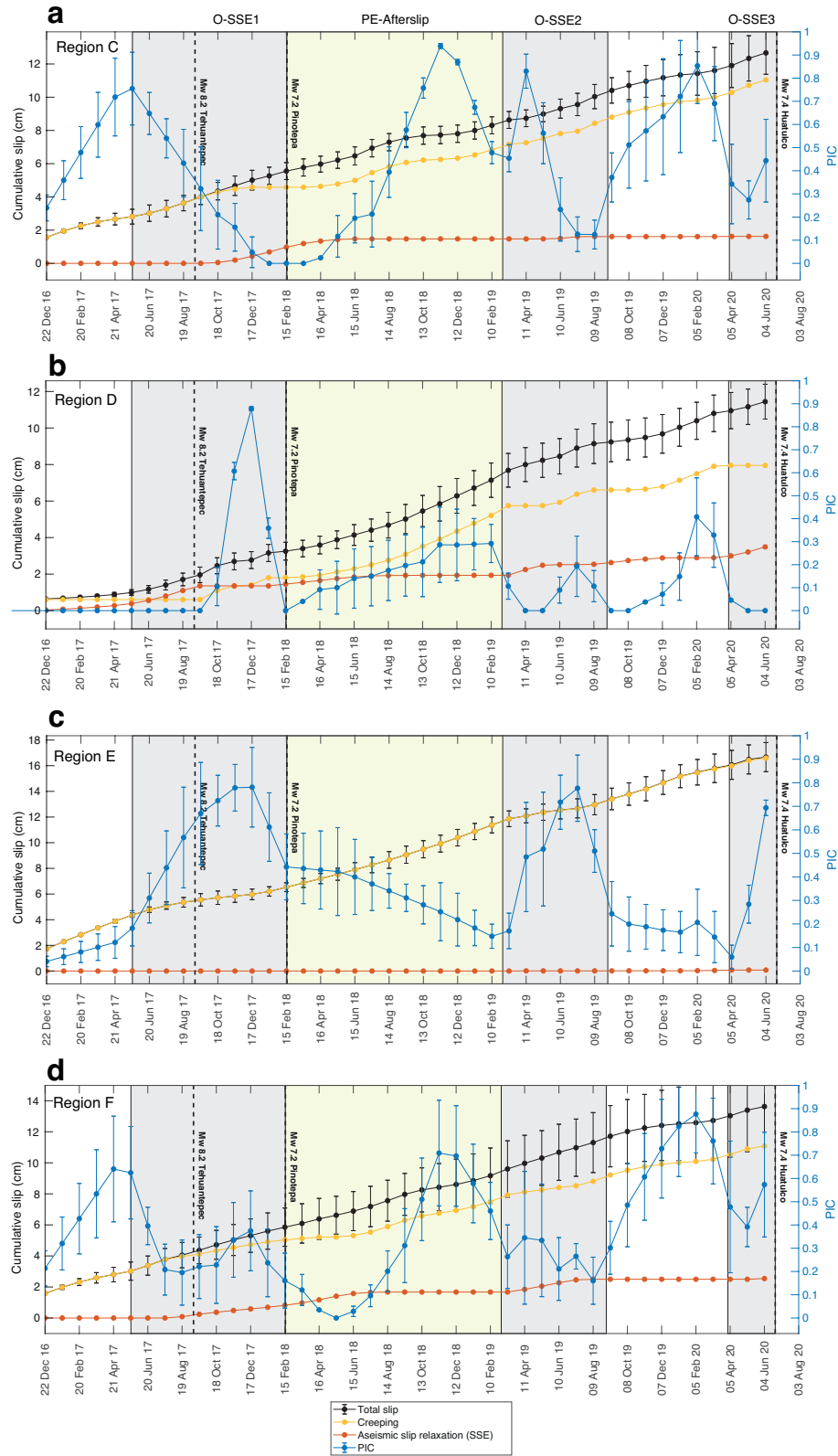


**Figure S12** Evolution of the cumulative total slip, creeping (slip under coupling regime), relaxing aseismic slip (SSEs and afterslip) and plate interface coupling (PIC) in regions C, D, E and F (see Figure 4).

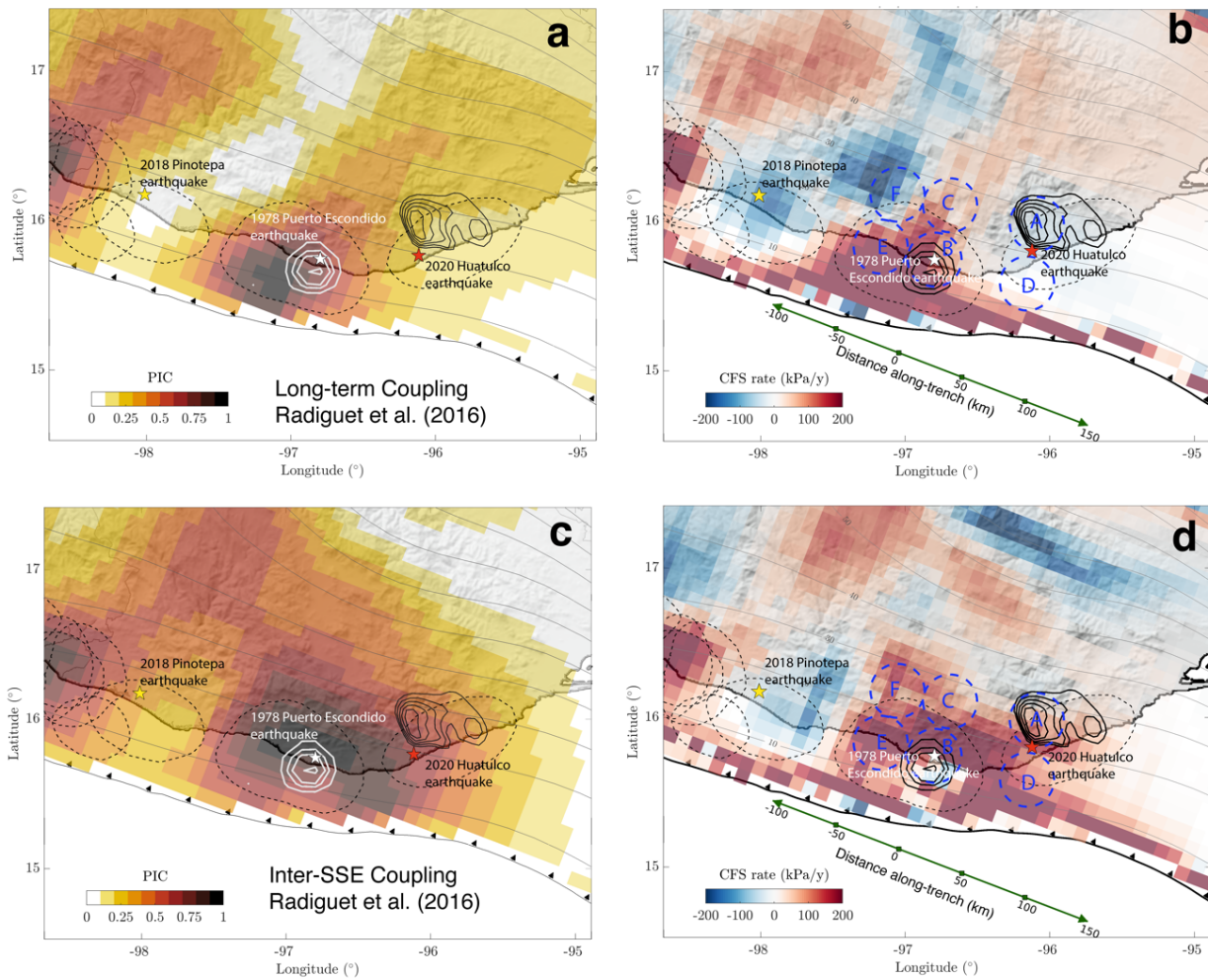


**Figure S13** Long-term and inter-SSE time-invariant interplate coupling models estimated by Radiguet et al. (2016) for the Oaxaca subduction zone and their associated CFS rates.

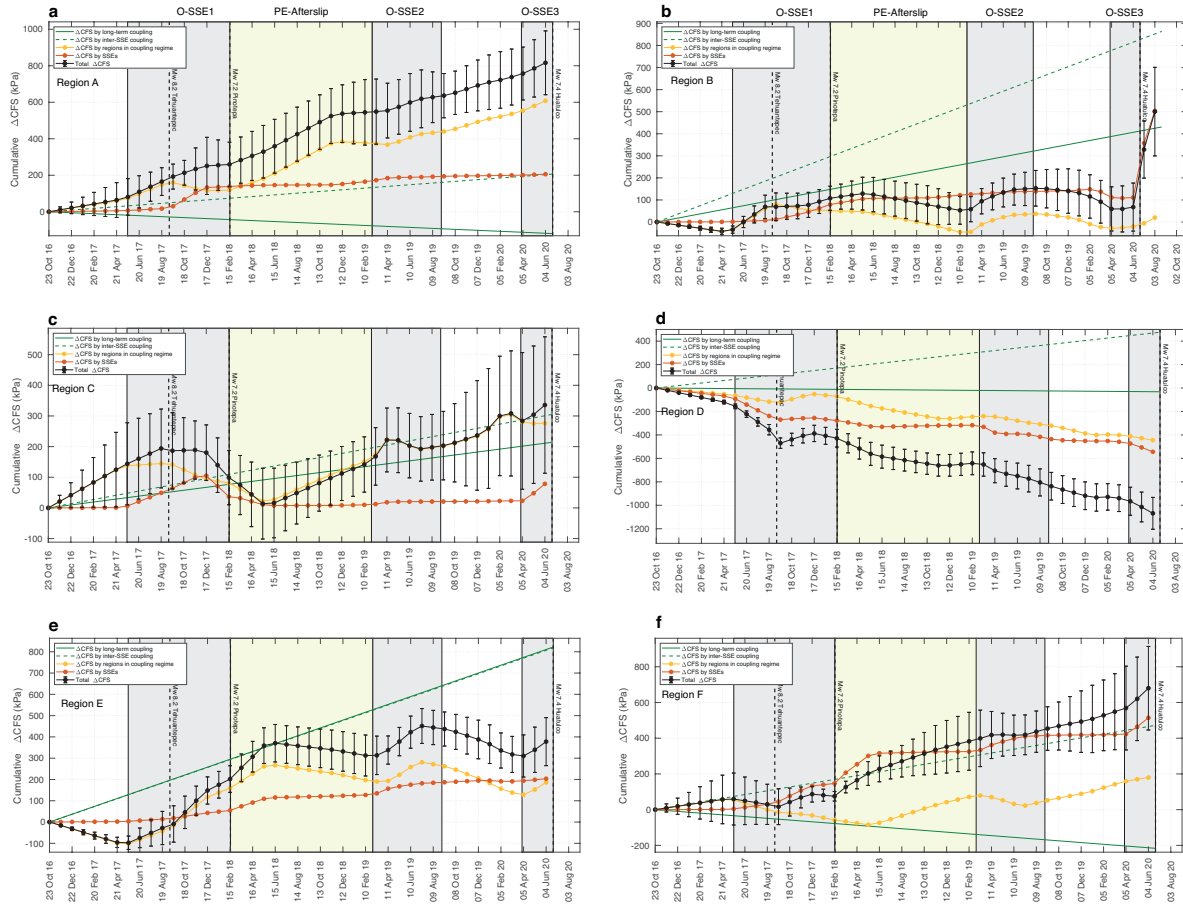


**Figure S14** Evolution of the stress partitioning in the seismogenic zone in Oaxaca. Every panel show the evolution of the total CFS (black curves) and their contributions from the relaxing aseismic slip (red curve) and coupled regions (yellow curve), for Regions A-F. Gray rectangles indicate the occurrence of SSEs in the region. The light-yellow rectangle shows the period when the postseismic afterslip of the 2018 Pinotepa and 2020 Huatulco earthquakes developed in the region.

## **Additional Supporting Information (Files uploaded separately)**

**Caption of Movie S1.** Evolution of the aseismic slip and the CFS in Oaxaca from May 2017 to August 2020 including the pre-seismic and postseismic phases of the 2020 Huatulco earthquake. Left panel show the aseismic slip rate evolution for the relaxing slip (in cm/yr) and the plate interface coupling (PIC) interpolated every 30 days. Right panel shows the accumulated CFS (in kPa) during 30 days prior to the date indicated in the upper part of the panel. Please notice the change of the colorbar scale in both aseismic slip rate and CFS after the occurrence of the 2020 Huatulco earthquake.

## **Supplementary References**

Bevis, M., Brown, A. Trajectory models and reference frames for crustal motion geodesy. *J*

*Geod* **88**, 283–311 (2014). <https://doi.org/10.1007/s00190-013-0685-5>.

Chen, C. W., & Zebker, H. A. (2000). Network approaches to two-dimensional phase unwrapping: intractability and two new algorithms. *JOSA A*, *17*(3), 401–414.

Cruz-Atienza, V.M., Tago, J., Villafuerte, C., Wei, M., Garza-Girón, R., Dominguez, L.A., Kostoglodov, V., Nishimura, T., Franco, S., Real, J., 2021. Short-Term Interaction between Silent and Devastating Earthquakes in Mexico. *Nature Communications*, DOI : 10.1038/s41467-021-22326-6.

DeMets, C., Gordon, R.G., Argus, D.F., 2010. Geologically current plate motions. *Geophysical Journal International* *181*, 1-80.

Farr, T. G., Rosen, P. A., Caro, E., Crippen, R., Duren, R., Hensley, S., ... Alsdorf, D. E. (2007). The shuttle radar topography mission. *Reviews of Geophysics*, *45*(2), 1–43.

Goldstein, R. M., & Werner, C. L. (1998). Radar interferogram filtering for geophysical applications. *Geophysical Research Letters*, *25*(21), 4035–4038.

<https://doi.org/10.1029/1998GL900033>

Hanssen, R. F. (2001). *Radar interferometry: data interpretation and error analysis* (Vol. 2).

Springer Science & Business Media.

- Heki K (2001) Seasonal modulation of interseismic strain buildup in Northeastern Japan driven by snow loads. *Science* 293:89–92.
- Lagler, K., Schindelegger, M., Böhm, J., Krásná, H., Nilsson, T., 2013. GPT2: Empirical slant delay model for radio space geodetic techniques. *Geophys Res Lett* 40, 1069-1073.
- Nikkhoo, M., Walter, T.R., 2015. Triangular dislocation: an analytical, artefact-free solution. *Geophysical Journal International* 201, 1119-1141.
- Radiguet, M., Perfettini, H., Cotte, N., Gualandi, A., Valette, B., Kostoglodov, V., Lhomme, T., Walpersdorf, A., Cabral Cano, E., Campillo, M., 2016. Triggering of the 2014 Mw7.3 Papanaoa earthquake by a slow slip event in Guerrero, Mexico. *Nature Geoscience* 9, 829-833.
- Rosen, P. A., Gurrola, E., Sacco, G. F., & Zebker, H. (2012). The InSAR scientific computing environment. *Synthetic Aperture Radar, 2012. EUSAR. 9th European Conference On*, 730–733.
- Savage, J.C., 1983. A dislocation model of strain accumulation and release at a subduction zone. *Journal of Geophysical Research: Solid Earth* 88, 4984-4996.
- Tago, J., Cruz-Atienza, V.M., Villafuerte, C., Nishimura, T., Kostoglodov, V., Real, J., Ito, Y., 2020. Adjoint Slip Inversion under a Constrained Optimization Framework: Revisiting the 2006 Guerrero Slow Slip Event. Accepted at *Geophysical Journal International*.
- Wang, R., Schurr, B., Milkereit, C., Shao, Z., Jin, M., 2011. An Improved Automatic Scheme for Empirical Baseline Correction of Digital Strong-Motion Records. *Bulletin of the Seismological Society of America* 101, 2029-2044.

